Received: 11 February 2024 | Revised: 31 October 2024 | Accepted: 27 November 2024

DOI: 10.1002/cac2.12636

CANCER COMMUNICATIONS Open Access

ORIGINAL ARTICLE

Radiotherapy-resistant prostate cancer cells escape immune checkpoint blockade through the senescence-related ataxia telangiectasia and Rad3-related protein

Chenyi Shao[1] | **Yingyi Zhang**[2,3] | **Hang Li**[1] | **Jiajia Chen**[4] | **Ting Huang**[1] | **Jiaze Li**[1] | **Simeng Wen**[5] | **Sen Wang**[1] | **Saijun Fan**[6] | **Yu Zhao**[1]

[1]Tianjin Key Laboratory of Radiation Medicine and Molecular Nuclear Medicine, Institute of Radiation Medicine, Chinese Academy of Medical Sciences and Peking Union Medical College, Tianjin, P. R. China

[2]School of Disaster and Emergency Medicine, Tianjin University, Tianjin, P. R. China

[3]Department of Biochemistry and Molecular Biology, Mayo Clinic College of Medicine, Rochester, Minnesota, USA

[4]Department of Oncology, Shengjing Hospital of China Medical University, Shenyang, Liaoning, P. R. China

[5]Department of Urology, The Second Hospital of Tianjin Medical University, Tianjin Medical University, Tianjin, P. R. China

[6]Institute of Radiation Medicine, Chinese Academy of Medical Sciences and Peking Union Medical College, Tianjin, P. R. China

Correspondence
Yu Zhao, Tianjin Key Laboratory of Radiation Medicine and Molecular Nuclear Medicine, Institute of Radiation Medicine, Chinese Academy of Medical Sciences and Peking Union Medical College, Tianjin, 300192, P. R. China.
Email: zhaoyu@irm-cams.ac.cn

Funding information
Nonprofit Central Research Institute Fund of the Chinese Academy of Medical Sciences, Grant/Award Number:

Abstract

Background: The majority of patients with prostate cancer (PCa) exhibit intrinsic resistance to immune checkpoint blockade (ICB) following radiotherapy (RT). This resistance is generally attributed to the limited antigen presentation of heterogeneous cells within tumors. Here, we aimed to isolate and characterize these diverse subgroups of tumor post-RT to understand the molecular mechanisms of their resistance to ICB.

Methods: Single-cell RNA-sequencing (scRNA-seq) was used to profile senescent cancer cell clusters induced by RT in LNCaP cells. The expression and

Abbreviations: CRPC, castration-resistant prostate cancer; PCa, prostate cancer; RT, radiotherapy; IR, irradiation; ICB, immune checkpoint blockade; scRNA-seq, single-cell RNA sequencing; TME, tumor microenvironment; APC, antigen-presenting cell; GEO, Gene Expression Omnibus; TCGA, The Cancer Genome Atlas; PRAD, prostate adenocarcinoma; FFPE, formalin-fixed paraffin-embedded; ATCC, American Type Culture Collection; FBS, fetal bovine serum; NSG, NOD.Cg-Prkdc^{scid}Il2rg^{Tm1Wjl}/SzJ; WT, wild-type; siRNA, small interfering RNA; shRNA, small hairpin RNA or short hairpin RNA; sgRNA, single guide RNA; DFS, disease-free survival; β-Gal, β-galactosidase; BSA, bovine serum albumin; GEM, gel bead-in-emulsion; UMI, unique molecular identifier; HVG, hypervariable gene; PCA, principal component analysis; UMAP, uniform manifold approximation and projection; GSVA, gene set variation analysis; ssGSEA, single-sample gene set enrichment analysis; GO, Gene Ontology; KEGG, Kyoto Encyclopedia of Genes and Genomes; IHC, immunohistochemistry; SI, staining index; TMA, tissue microarray; ATRi, ATR inhibitor; PCR, polymerase chain reaction; RT–qPCR, real-time quantitative PCR; IF, Immunofluorescence; FACS, fluorescence-activated cell sorting; IP, immunoprecipitation; HPLC, high-pressure liquid chromatography; PPλ, phosphatase λ; Baf-A1, bafilomycin A1; MHC, major histocompatibility complex; ATR, ataxia telangiectasia and Rad3-related protein; ATM, ataxia telangiectasia mutated; CDKN1A, cyclin-dependent kinase inhibitor 1A; CDKN2A, cyclin-dependent kinase inhibitor 2A; PARP1, Poly (ADP-ribose) polymerase 1; PRKDC, protein kinase; MARCH1, membrane-associated ring-CH-type finger 1; PTM, posttranslational modification; IgV, immunoglobulin variable domain; IgC, immunoglobulin constant domain; EC, extracellular cadherin; TM, transmembrane domain.

Chenyi Shao, Yingyi Zhang, Hang Li, and Jiajia Chen contributed equally.

2021-RC310-010; National Natural Science Foundation of China, Grant/Award Numbers: 81972654, 81730086; CAMS Innovation Fund for Medical Sciences, Grant/Award Numbers: 2021-I2M-1-042, 2021-I2M-1-060; Tianjin International Student Science and Technology Activities, Grant/Award Number: 20160014

phosphorylation levels of ataxia telangiectasia and Rad3-related protein (ATR) were assessed by immunohistochemistry in clinical samples from patients with or without RT. Co-immunoprecipitation, mutagenesis, and Western blotting were used to measure the interactions between proteins. Xenograft experiments were performed to assess the tumor immune response in the mice.

Results: We identified a subset of PCa cells that exhibited resistance to RT, characterized by a reduced antigen presentation capability, which enhanced their ability to evade immune detection and resist cytotoxic T-lymphocyte-associated protein 4 (CTLA-4) blockade. scRNA-seq revealed that the senescent state was a transient phase of PCa cells post-RT, particularly in CTLA-4 blockade treatment-resistant cells. This state was marked by increased cytosolic ATR level. Cytosolic ATR phosphorylated CD86 in its cytosolic domain and enhanced the interaction between CD86 and its E3 ligase MARCH1 through electrostatic attraction. Depletion or inhibition of Atr increased the sensitivity to immune attack and improved responses to anti-Ctla-4 antibody treatment in a mouse model.

Conclusions: Our findings indicate that the activation of cytosolic ATR, which is associated with cellular senescence, impedes the effectiveness of combined RT and ICB treatments. This discovery may provide valuable insights for improving the efficacy of combined RT and ICB therapies in PCa.

KEYWORDS
ATR, CD86, immune checkpoint, senescence

1 | BACKGROUND

Immune checkpoint blockade (ICB) targeting programmed death-1 (PD-1)/programmed death ligand 1 (PD-L1) and cytotoxic T-lymphocyte-associated protein 4 (CTLA-4) has shown promise in cancer treatment, with a subset of patients experiencing positive outcomes [1, 2]. However, the majority of patients with "cold" tumors exhibit resistance to ICB due to a paucity of antigen presentation and immune responses. Immunotherapy has been combined with radiotherapy (RT) to improve patient survival, a strategy that has shown efficacy across various cancer types [3]. In addition to its cytotoxic effects, RT modulates the immune system, as evidenced by increased cytokine and chemokine expression in breast cancer [4] and melanoma [5]; the abscopal effect in melanoma [6]; T cell activation in lung cancer [7, 8]; dendritic cell activation in colorectal cancer [9]; and enhanced antigen-specific effector cell trafficking in melanoma [10]. High-dose radiation is known to bolster both innate and adaptive immune responses by activating DNA-sensing pathways in tumor cells, as observed in breast [11] and colorectal cancers [12]. Conversely, low-dose RT in conjunction with immunotherapy can induce inflammation, leading to the regression of metastatic ovarian tumors [13]. Fractionated RT has been shown to stimulate systemic antitumor immunity and, when combined with ICB, can eradicate distal metastases in patients with breast cancer [14], colorectal carcinoma [15], melanoma [16], or pancreatic cancer [17, 18]. An analysis of the tumor microenvironment (TME) revealed that RT enhances T-cell production, infiltration, recognition, and effector function [3, 19]. However, clinical trials have shown that the efficacy of ICB in "cold" tumors, such as prostate, bladder, and kidney cancers, is limited, with only a small subset of patients benefiting [20]. In a phase I/II trial [21], the combined treatment of ipilimumab with RT resulted in a 16% decrease in prostate-specific antigen (PSA) levels in patients with metastatic castration-resistant prostate cancer (mCRPC) [22]. Combination therapy in phase III trial of patients with mCRPC did not produce an overall survival advantage over the placebo [23, 24]. The molecular resistance mechanism of combined RT and ICB therapy in prostate cancer (PCa) cells remains poorly understood.

The shaping of the differentiation pathway of naïve T cells by antigen-presenting cells (APCs) and cancer cells depends on the first activation signals. T cells are typically activated when the T-cell receptor interacts with a specific antigen on the major histocompatibility complex

(MHC) molecule and when certain costimulatory signals, especially those from the B7 family, are expressed. The interaction between B7-1 (CD80) or B7-2 (CD86) on cancer cells and CD28 on T cells is crucial for immunotherapy with ipilimumab. The loss of these interactions is a significant factor contributing to the insensitivity of cancer cells to ipilimumab treatment [25, 26]. The process of CD86 induction is more rapid than that of CD80 induction. CD86 induction typically begins within 6 hours of stimulation and peaks between 18 and 24 hours in macrophages and APCs [27, 28]. However, CD80 induction peaks at 48-72 hours [29]. Hence, the transient expression of CD86 may be regulated by rapid degradation, but the precise mechanism remains elusive.

In this study, we aimed to identify the pathways mediating the loss of an immune reaction in RT-resistant PCa cells, with a focus on intrinsic cellular factors. Single-cell RNA sequencing (scRNA-seq) was employed to characterize the cellular heterogeneity within PCa cell populations, and resistance-related molecular mechanisms were investigated using cellular and mouse models. An explanation of the resistance pathway will provide new insights into the potential mechanism of ICB in PCa.

2 | MATERIALS AND METHODS

2.1 | The cancer genome atlas (TCGA) cohort and the second hosipital of tianjin medical university cohort

The expression profiles and clinical characteristics of prostate adenocarcinoma (PRAD) from TCGA were used for analysis. Data were obtained using the "TCGAbiolinks" package (version 2.32.0, https://bioconductor.org/packages/release/bioc/html/TCGAbiolinks.html) [30]. A total of 246 cases with transcriptome profiling were downloaded, of which 83 cases were clinically informative [31].

For the analysis of the Second Hosipital of Tianjin Medical University cohort, the study was approved by the Tianjin Medical University Institutional Review Board. Tissues were obtained from the Tianjin Medical University Tissue Registry. A total of 302 formalin-fixed, paraffin-embedded (FFPE) samples of hormone-naïve primary PCa and bone metastatic PCa were collected for RNA extraction and immunohistochemical (IHC) staining. Clinical information of the patients was also collected. Among the 302 cases, 142 cases with no significant tumor regression or even progression post-RT completion were classified into the RT-resistant group. For senescence analysis in the RT-resistant cohort, the cohort was divided into two groups by the median RNA level of *CDKN1A* or *CDKN2A* (n = 71 for each group). The overlap of the $CDKN1A^{high}$ group and the $CDKN2A^{high}$ group was considered the $CDKN1A^{high}/CDKN2A^{high}$ group (n = 60). Similarly, $CDKN1A^{low}/CDKN2A^{low}$ was defined in the same manner (n = 36). The $CDKN1A^{high}/CDKN2A^{high}$ group and $CDKN1A^{low}/CDKN2A^{low}$ group paired samples were used for IHC assay. Detailed patient information is described in Supplementary Table S1.

2.2 | Identification of differentially expressed genes (DEGs) and gene enrichment analysis

The DESeq2 package (version 1.42.0, https://bioconductor.org/packages/release/bioc/html/DESeq2.html) [32] in R (version 4.1.2, https://cran.rstudio.com/bin/windows/base/old/) was used to identify the DEGs with the default settings. DEGs were identified according to a P value < 0.05 and $|\log_2 FC| > 0.5$.

The clusterProfiler package (version 4.10.0, https://www.bioconductor.org/packages/release/bioc/html/clusterProfiler.html) [33] was used to analyze the molecular and functional characteristics of the DEGs. Upregulated and downregulated DEGs were enriched in the Gene Ontology (GO) database. The P value was calculated by Fisher's exact test and adjusted for multiple testing using the Benjamini–Hochberg method. The Q value was calculated by adjusting the P value using the Storey method. An adjusted P value < 0.05 and a Q value < 0.05 were considered statistically significant. The rich factor is the ratio of the number of enriched DEGs in the pathway to all genes annotated in the pathway.

2.3 | Cell culture

The human PCa cell lines LNCaP and PC-3, the murine PCa cell line RM1, and the human embryonic kidney (HEK) 293 cell line were purchased from the American Type Culture Collection (ATCC) (Manassas, VA, USA). The murine PCa cell line TRAMP-C1 was a gift from Dr. Yuanjie Niu at the Second Hospital of Tianjin Medical University (Tianjin, China). LNCaP cells, PC-3 cells, and RM1 cells were cultured in 10% (v/v) fetal bovine serum (FBS) (16000044, Gibco, Grand Island, NY, USA)-containing RPMI 1640 medium (C3010-0500, VivaCell, Shanghai, China). TRAMP-C1 cells and HEK293 cells were cultured in DMEM (C3113-0500, VivaCell) supplemented with 10% (v/v) FBS. The cells were maintained in a humid atmosphere containing 5% CO_2 at 37°C.

2.4 | Mouse xenograft generation

All animal experiments were performed with the approval of the Laboratory Animal Ethics Committee of the Institute of Radiation Medicine, Chinese Academy of Medical Sciences (approval number: IRM-DWLL-2023033) and in accordance with the animal ethical review guidelines. All the mice were purchased from Beijing Vital River Laboratory Animal Technology Co., Ltd. (China) and maintained under specific pathogen-free (SPF) conditions under the general requirements for animal experiments (GB/T 35823-2018). The mice were housed for a 2-week period to acclimate before being used in experiments.

Grafts were generated from 6-week-old male NOD.Cg-Prkdc^{scid}Il2rg^{Tm1Wjl}/SzJ (NSG) mice to obviate interference from the immune microenvironment. RT-resistant xenografts were generated on one side, and control xenografts were generated on the other side of each mouse, as described below. A total of 5×10^6 TRAMP-C1 cells in 100 μL of PBS with 100 μL of Matrigel matrix (HY-356234, BD Bioscience, Franklin Lakes, NJ, USA) were injected into one flank of each NSG mouse. The tumor on one flank was exposed to 2 fractions of 5 Gy of X-ray radiation at 14 days after the injection to generate RT-resistant xenografts. The tumor on the other flank without irradiation served as a control. Mice were euthanized with CO_2 when the maximum tumor volume was 400 mm^3. The implanted tumors were manually dissected into 5 mm^3 pieces using a sterile scalpel blade and stored in transport medium at 4 °C until xenograft preparation. The second-generation xenograft was produced in 6-week-old male wild-type (WT) C57BL/6 mice for immune function measurements. TRAMP-C1 cells, either uninfected or infected with lentiviruses expressing short hairpin RNAs (shRNAs) and/or recombinant expression vectors, were utilized to establish xenograft tumors in accordance with the experimental protocol.

2.5 | Irradiation treatment of the mice

Eight-week-old male NSG mice were subjected to 225 kVp and 17 mA X-rays at a dosage rate of 2 Gy/min using an RS2000 radiator (RAD Source Technologies, Suwanee, GA, USA). The right flank tumors (400 mm^3) were exposed to a total of 10 Gy of X-rays via two 5 Gy irradiations. The exposure field was chosen based on the size of the irradiated tumor to expose the entire tumor of the mouse, and a dosimeter was placed in this field to detect the dosage rate. Radiation was focused using a collimator of 4 × 4 cm or 2 × 2 cm, depending on the location.

2.6 | Immunotherapy experiments

Operative tumor tissue from NSG mice was mechanically disaggregated, triturated through a 1 mL syringe, and mixed 1:1 with Matrigel matrix (HY-356234, BD Bioscience). A total of 200 μL of the mixture was injected into the flank of a 6-week-old C57BL/6 male WT mouse. The size of the tumors and the state of the mice were measured. For immunotherapy administration, mice bearing 100 mm^3 tumors were randomized into different groups and intraperitoneally injected with an anti-mouse Ctla-4 antibody (9D9) (200 μg, HY-P99132, MedChemExpress, Monmouth Junction, NJ, USA) or IgG2a (HY-P99978, MedChemExpress) on days 7, 10, and 13. Subsequently, tumor growth was measured with calipers every 7 days. Mice were euthanized, and tumors were collected from all animals once the tumors reached a volume of 400 mm^3.

2.7 | Survival analysis

The survival analysis of TCGA-PRAD was performed using the website of GEPIA (http://gepia.cancer-pku.cn/). The *ATR* and *ATM* expression and disease-free survival (DFS) of patients were used for the analysis with quartile cutoff.

For the cohort from the Second Hospital of Tianjin Medical University and the corresponding mouse survival analysis, the survival package (version 3.5-7, https://rdrr.io/cran/survival/) and the survminer package (version 0.4.9, https://github.com/kassambara/survminer) in R were used to construct survival curves and perform statistical analysis. The data were analyzed via Kaplan–Meier analysis and the log-rank test. A P value less than 0.05 was considered statistically significant. IHC staining results of CD8 were used to assess the CD8$^+$ T cells infiltration ratio, and Real-time quantitative PCR (RT-qPCR) were used to evaluated the *ATR* expression levels. In PCa patients, the endpoint for survival analysis was defined by the occurrence of biochemical recurrence, characterized by a 2 ng/mL increase in post-treatment PSA levels after radical radiotherapy completion [34]. Data were analyzed with median cutoff point. The data are presented as median survival times with 95% confidence intervals.

In the mouse survival analysis, the time taken for the tumor to grow to a volume of 400 mm^3 was recorded as the survival time and was used for analysis.

2.8 | Irradiation of cells

LNCaP, PC-3, TRAMP-C1, and RM1 cells (8×10^6) were seeded in a 15 cm dish and cultivated for 24 h in complete

medium containing 10% FBS prior to irradiation. For γ-ray irradiation, a Gammacell-40 ^{137}Cs irradiator (Atomic Energy of Canada Limited, Chalk River, ON, Canada) with a dosage rate of 0.8 Gy per minute was employed. A single dose of 10 Gy was administered to LNCaP, PC-3, TRAMP-C1, and RM1 cells.

Senescent cells were generated by irradiation followed by maintenance culture for 10 days as previously reported [35], and the cells were harvested on day 10 for protein expression and interactions analysis using Western blotting, Co-IP, etc. The immune checkpoints expression was determined on day 14 using fluorescence-activated cell sorting (FACS) assay [36]. The cells without irradiation were cultured for 1 day and served as a negative control.

2.9 | Western blotting and cellular fractionation

Western blotting was performed as previously described [37]. Briefly, the total proteins were obtained from cells using RIPA buffer (R0010, Solarbio, Beijing, China). Cellular subcomponent proteins were isolated and extracted using Cell Fractionation Kit (78840, Thermo Fisher Scientific, Waltham, MA, USA) according to the manual instructions. The protein concentration was quantified with a BCA protein quantification assay (A55864, Thermo Fisher Scientific). Equal amounts of protein samples were mixed with 5× loading buffer (P1040, Solarbio) and boiled for 15 min. The samples were separated on an SDS–PAGE gel and transferred to a nitrocellulose membrane (24937-79-9, Millipore, Billerica, MA, USA). The membrane was blocked with 5% milk (D8340, Solarbio) for 1 h at room temperature and then incubated with the primary antibody at 4°C overnight. The membrane was washed with 1 × TBST three times the next day and incubated with peroxidase-conjugated secondary antibodies for 1 h at room temperature. The protein bands were visualized with SuperSignal West Pico PLUS Chemiluminescent Substrate (PI34577, Thermo Fisher Scientific). The antibodies used are shown in Supplementary Table S2.

2.10 | β-Galactosidase (β-Gal) staining

A β-Gal staining assay was performed using a Senescence β-Galactosidase Staining Kit (C0602, Beyotime Biotechnology, Shanghai, China) according to the manufacturer's protocol [38]. Briefly, the cells were fixed with fixative solution for 15 min at room temperature and washed three times with PBS. The β-Gal staining solution was prepared according to the instructions and incubated with the cells overnight at 37°C. The samples were observed under an optical microscope, and the senescent cells were dyed blue.

2.11 | scRNA-seq analysis

The scRNA-seq datasets can be found in the online repositories of Gene Expression Omnibus (GEO) (GSE234387). For sample preparation, LNCaP cells were divided into two groups and seeded at a density of 1×10^5 cells/cm^2 24 h prior to treatment ($n = 3$ for each group). Then, the cells were exposed to 2 Gy of ionizing radiation. After 7 days of culture, the unirradiated or RT-resistant cells (> 70% β-Gal staining) were digested with 0.25% (w/v) trypsin (25200072, Gibco) and collected by centrifugation at 300 × g for 4 min at room temperature for subsequent analysis. Samples with ≥ 90% living cells were analyzed.

2.12 | Library construction for scRNA-seq

The whole transcriptomic information of each sample was captured with 10× Genomics Chromium™ (Pleasanton, CA, USA) according to the manufacturer's protocol [39]. Briefly, for gel bead-in-emulsion (GEM) generation and barcoding, the concentration of the cellular suspensions was adjusted to 1×10^4 cells/μL in PBS containing 0.04% bovine serum albumin (BSA) (11020039, Thermo Fisher Scientific). According to the manufacturer's protocol for the Chromium Next GEM Chip G Single Cell Kit (PN1000120, 10× Genomics), a reaction system including 75 μL of Master Mix with a cell suspension, 40 μL of gel beads containing barcode information, and 280 μL of oil drops was added to the wells of Rows 1, 2, and 3 for loading onto Chromium Next GEM Chip G. Approximately 10,000-16,000 cells were loaded per reaction, resulting in a recovery of approximately 6,000-10,000 cells. The chip was subsequently loaded on the Chromium Controller to generate single-cell GEMs. The released mRNAs were transcribed into cDNAs with an Illumina® R1 sequence, a 16 nt 10× barcode, a 10 nt unique molecular identifier (UMI), and a poly-dT primer sequence by reverse transcription. The program was as follows: 53°C for 45 min, 85°C for 5 min, and a held at 4°C. The reactions were performed on a Bio-Rad C1000 Touch instrument.

For cDNA amplification, Recovery Agent and Dynabeads Cleanup Mix were used to clean the products from the previous experiment. The full-length cDNAs were amplified by PCR. A total of 35 μL of clean product was mixed with 15 μL of Feature cDNA Primers 1 and 50 μL of Amp mix. The mixture was incubated with a thermal cycler at 98°C for 3 min, followed by 11 cycles of 98°C for 15 s, 63°C for 20 s, 72°C for 60 s, 72°C for 60 s, and a hold at 4°C. The amplification products were cleaned using the SPRIselect reagent.

For 3' gene expression library construction, the experiment was performed according to the manufacturer's

instructions for the Chromium Next GEM Single Cell 3' Reagent Kit v3.1 (PN-1000121, 10× Genomics). The cDNA was first digested into 200-300 bp fragments using a thermocycler. Before PCR, the thermal cycler was precooled at 4°C. For cDNA digestion, a total of 10 μL of purified cDNA sample was mixed with 5 μL of fragmentation buffer, 10 μL of fragmentation enzyme, and 25 μL of Buffer EB and then processed at 32°C for 5 min, 65°C for 30 min, and held at 4°C. An SPRI select Reagent Kit (0.6× SPRI and 0.8× SPRI) was used to select fragments, perform end repair, and perform A-tailing. Then, a PCR was set up to perform adaptor ligation with a reaction of 50 μL of sample, 20 μL of ligation buffer, 10 μL of DNA ligase, and 20 μL of Adaptor Oligos. The thermal cycler was heated at 20°C for 15 min and held at 4°C. Then, 0.8× SPRI was used for adaptor ligation selection. A PCR mixture containing 30 μL of sample, 10 μL of SI primer, and 50 μL of AmpMix was used to add the sample index. The mixture was incubated in a thermal cycler with the following protocol: 98°C for 45 s; 5 cycles of 98°C for 20 s, 54°C for 30 s, and 72°C for 20 s; 72°C for 1 min; and a hold at 4°C. Next, 0.6× SPRI and 0.8× SPRI were used for double-sided size selection. Finally, fragments containing connector sequences, including R1, R2, P5, P7, and the sample index, were produced. The insert size of the library was examined using an Agilent 2100 system. The effective concentration and quantification of the library were performed with a Qubit 3.0 instrument.

2.13 | scRNA-seq sequencing

Sequencing of the constructed library was subsequently performed on the Illumina NovaSeq 6000 platform with a depth of 20,000 reads per cell and 150-bp (PE150) paired-end reads. The 16 nt barcodes and 10 nt UMI at the terminus of Read1 were used to quantify the number of cells and gene expression, respectively. The cDNA at the terminus of Read2 was aligned with the reference genome.

2.14 | Read alignment

Reads with mismatched barcodes, UMIs containing mono-oligo chains, unknown bases (N), low-quality bases (Q <10), or UMI counts < m×10% barcodes were filtered with 10× Genomics Cell Ranger software (version 3.1.0, 10× Genomics). The clean reads were then mapped to the human genome (hg38).

2.15 | scRNA-seq data processing

Seurat software (version 3.1.1, 10× Genomics) was used for the downstream analysis [40]. The cells whose unique feature counts were greater than 2,500 or less than 200 and whose mitochondrial gene percentage was greater than 30% were filtered for quality control. The level of cell expression was normalized using the log normalization method (scale. factor = 10,000). A total of 2,000 hypervariable genes (HVGs) were selected using the "vst" method via the FindVariableFeatures function. The ScaleData function was used to perform the z score conversion of the data, and then the dimensionality reduction of the data was performed via principal component analysis (PCA) (dimensions = 1: 10). The function FindNeighbors from the Seurat package was used to calculate the distance between each cell with the default parameters (dimensions = 1: 10). The cells were clustered using the FindClusters function with a resolution value of 0.5. Uniform manifold approximation and projection (UMAP) was used to obtain a two-dimensional representation for data visualization.

2.16 | Marker gene expression analysis

The differentially expressed marker genes between clusters were analyzed with the function FindAllMarkers. Genes expressed in at least 25% of the cluster with P values less than 0.05 and average fold changes greater than 0.25 were identified as significantly differentially expressed genes and were used for Gene Ontology (GO) analysis and Kyoto Encyclopedia of Genes and Genomes (KEGG) analysis. The GOplot package (version 1.0.2, https://wencke.github.io/), the clusterProfiler package (version 4.10.0), and the org.Hs.eg.db package (version 3.17.0, https://github.com/bioconda/bioconda-recipes/tree/master/recipes/bioconductor-org.hs.eg.db) were used for the GO analysis and KEGG analysis. The Benjamini–Hochberg method was used to adjust the P values. Terms with a P value <0.05 and a Q value < 0.01 were considered significant.

2.17 | Pseudotime analysis

For the single-cell trajectory analysis, 10,000 random cells were selected, and positive marker genes for each cluster were used to establish pseudotime trajectories with DDRTree. Analyses were performed using Monocle 2 (version 2.28.0, https://cole-trapnell-lab.github.io/monocle-release/), with the default parameters of a minimum limited detection value of 0.5 and a minimum index of 0.1.

2.18 | Gene set variation analysis (GSVA)

GSVA was performed to estimate the drift of the genes among the cell clusters [41]. The average gene expression of

each cluster was calculated and used for analysis with the GSVA package (version 1.52.2, https://www.bioconductor.org/packages/release/bioc/html/GSVA.html) and the default parameters. Gene sets of human immunologic signature (C7), cell division (Systematic name: M1727) and epithelial cell proliferation (Systematic name: M15437) were downloaded from the Molecular Signature Database (MSigDB, https://www.gsea-msigdb.org/gsea/msigdb).

2.19 | Analysis of immune cell infiltration

The xCell package (version 1.1.0, https://comphealth.ucsf.edu/app/xcell) [42] was used to calculate the infiltration levels of immune cells via single-sample gene set enrichment analysis (ssGSEA). The expression profiles of TCGA-PRAD cohort were analyzed.

2.20 | IHC staining

FFPE tissue samples were cut into 5-μm-thick sections. The experiment was performed using an UltraSensitive S-P (Rabbit) IHC Kit (13079S, Cell Signaling Technology, Boston, MA, USA). All procedures were performed in accordance with the manufacturer's instructions. Briefly, the sections were deparaffinized in xylene and rehydrated in a graded ethanol series according to standard protocols. Antigen retrieval was performed using an unmasking solution at 4°C for 15 min. Endogenous peroxidase activity was quenched via an incubation with 3% H_2O_2 for 15 min. The sections were blocked with normal goat serum (C0265, Beyotime) and incubated for 2 h. Then, the sections were incubated with primary antibodies, including CD8 (1:20000 dilution; 66868-1, proteintech, Wuhan, Hubei, China), ATR (1:200 dilution; PA5-85507, Invitrogen, Carlsbad, CA, USA), p-ATR-T1989 (1:250 dilution; ab28936, Abcam, Cambridge, MA, USA), CD86 (1:200 dilution; sc-28347, Santa Cruz Biotechnology, Dallas, TX, USA) and ATM (1:200 dilution; sc-377293, Santa Cruz Biotechnology), at 4°C overnight. The sections were washed with PBS three times and incubated with goat anti-rabbit HRP (1:200 dilution; 8114, Cell Signaling Technology) at 37°C for 1 h. Then, the sections were washed with PBS every 5 min for three times. 3,3′-Diaminobenzidine (DAB-2031, Transgene, Beijing, China) was used to visualize the antibody-bound antigen. Images were acquired randomly from a 40× field and analyzed with Image-Pro Plus software (Media Cybernetics, MD, USA).

IHC staining was scored by three investigators, including a GU pathologist, to quantify the staining of each protein. The staining index (SI) was calculated as follows: the staining intensity and percentage of positive staining (stained cells/total cells) for any given tissue microarray (TMA) spot were graded individually. For the staining intensity, no obvious staining was scored as 0, light yellow staining was scored as 1, brownish-yellow staining was scored as 2, and brown staining was scored as 3. For the percentage of positive staining, scores were assigned as follows: 0% = 0, 1%-30% = 1, 31%-60% = 2, and 61%-100% = 3. The final SI score for each TMA element was obtained by multiplying the values obtained from the staining intensity and percentage (SI = staining intensity × positive staining percentage) and was used for the correlation analysis. Samples with SI scores were ranked into three grades: low, 0-3; intermediate, 4-6; high, 7-9, respectively. For CD8 staining assay, over 3 foci/slide was identified as high $CD8^+$ T cells infiltration ratio; 0-2 foci/slide was identified as low ratio [43]. The antibodies used are listed in Supplementary Table S2.

2.21 | FACS assay

The cells were isolated with trypsin and suspended in PBS. The extra-membranous antigens, including CD86, Cd86, MHC II, Mhc II, Cd326, Cd3, and Cd8, were analyzed using the protocols described below. Approximately 1×10^5 cells were incubated with APC-conjugated CD86 (clone: IT2.2; 305411, Biolegend, San Diego, CA, USA), FITC-conjugated Cd86 (clone: GL-1; 105005, Biolegend), MHC II (ab55152, Abcam), Mhc II (ab139365, Abcam), Percp/Cyanine5.5-conjugated Cd326 (clone: G8.8; 118219, Biolegend), APC-conjugated Cd3 (clone: 17A2; 100235, Biolegend), and PE-conjugated Cd8 (clone: 53-6.7; 100708, Biolegend) antibodies for 30 min in the dark on ice. The cells were washed three times with PBS. Human MHC II and mouse Mhc II antibodies were hybridized with Alexa Fluor 488-conjugated goat anti-mouse IgG (H+L) (A-10680, Thermo Fisher Scientific) and YSFluor™488-conjugated donkey anti-rat IgG (H+L) (34406ES60, Yeasen, Shanghai, China) at 4°C for 30 min, respectively. Afterward, the cells were washed three times with PBS and collected by centrifugation at 300 ×g for 4 min at room temperature. The PBS was discarded, and the cells were then fixed in 4% paraformaldehyde (P1110, Solarbio) for 15 min and washed with PBS three times. The number of PBS-resuspended samples was determined with a BD FACSCanto II system flow cytometer and analyzed with FlowJo software (https://www.flowjo.com/).

For mouse tissue samples, tumors were cut into small pieces (1 mm) and digested with 2 mg/mL collagenase (9001-12-1, Sigma–Aldrich, St. Louis, MO, USA) in DMEM for 1 h at 37°C. The cells were filtered through a 45 μm nylon strainer and resuspended in red blood cell lysis

buffer (420301, Biolegend) for 3 min at room temperature. After centrifugation, the cells were then suspended in PBS with 2% BSA and costained with the following antibodies for 1 h at room temperature: APC-conjugated Cd45 antibody (clone: 30-F11; 103112, Biolegend), FITC-conjugated Cd4 antibody (clone: RM4-5; 100510, Biolegend), and PE-conjugated Cd8 antibody (clone: 53-6.7; 100708, Biolegend). Then, the cells were washed with PBS three times and analyzed on a flow cytometer.

2.22 | Human PCa specimens and RNA extraction from human tissues

Total RNA was extracted from FFPE tissues using a RecoverAll Total Nucleic Acid Isolation Kit (AM1975, Thermo Fisher Scientific) according to the manufacturer's protocol. Briefly, 80 μm thick FFPE tissues were mixed with 1 mL of 100% xylene and incubated at 50°C for 3 min to remove the paraffin. The tissues containing total nucleic acid without paraffin were collected by centrifugation at 12,000 ×g for 2 min. The precipitate was washed twice with 1 mL of 100% ethanol. The precipitate was dried in air for 5 min to remove the residual ethanol. The extracted tissues were subsequently digested with 200 μL of digestion buffer and 4 μL of protease. RNA was extracted from the tissues by an incubation at 50°C for 15 min and then at 80°C for 15 min. The RNA was collected into a filter cartridge after being mixed with the isolation additive/ethanol mixture and centrifuged at 10,000 ×g for 1 min. The filter cartridge was washed with wash buffers 1, 2, and 3, according to the manufacturer's instructions. The remaining DNA was then removed via an incubation with DNase for 30 min. The filter cartridge was washed with wash buffers 1, 2, and 3 again, and the clean RNA was eluted with nuclease-free water. The quality and amount of RNA were estimated using YSNano-100 (80481ES03, Yeasen).

2.23 | RNA extraction from cultured cells

Total RNA was extracted using TRIzol reagent (15596026, Invitrogen). Approximately 5×10^6 cells were lysed in 1 mL of TRIzol through vortexing and left to stand for 10 min. Chloroform (200 μL, C2432, Sighma-Aldrich) was added to the lysate to separate the organic phase. The mixture was vortexed and incubated for 10 min. The upper aqueous phase containing RNA was collected by centrifugation at 12,000 × g for 15 min at 4°C and transferred to new sterile, enzyme-free centrifuge tubes. An equal volume of isopropanol (I811932, MACKLIN, Shanghai, China) was added to precipitate the RNA. The RNA was collected by centrifugation at 12,000 × g for 15 min at 4°C. The samples were washed twice with 75% ethanol. The ethanol was discarded and the pellet was dried in air at room temperature for 5 min. The fresh RNA was dissolved in sterile, enzyme-free water and assessed using a YSNano-100 system.

2.24 | Reverse transcription PCR (RT–PCR)

A total of 1 μg of RNA was reverse transcribed into cDNA using the PrimeScript Reverse Transcriptase Kit (RR037A; Takara Bio, Kyoto, Japan). Briefly, a 20 μL reaction system containing 1 μg of RNA, 4 μL of 5×PrimeScript Buffer, 1 μL of PrimeScript RT Enzyme Mix I, 1 mL of Oligo dT Primer (50 μmol/L), 1 μL of random 6-mers, and RNase-free ddH_2O was incubated in an Applied Biosystems SimpliAmp PCR system (A24811, Thermo Fisher Scientific) under the following conditions: 37°C for 15 min; 85°C for 5 s; and maintained at 4°C.

2.25 | RT–qPCR

Hieff UNICON® Universal Blue qPCR SYBR Green Master Mix (11184ES08, Yeasen) was used for real-time PCR, with a reaction system of 20 μL containing 25 ng of cDNA, 0.4 μL of forward primer (10 μmol/L) and 0.4 μL of reverse primer (10 μmol/L) per well. The reactions were performed on a Celemetor 96 (80520ES03, Yeasen) with a program of 1 cycle of 95°C for 2 min; 50 cycles of 95°C for 10 s and 60°C for 30 s; and 1 cycle of a melting curve analysis with a temperature increase rate of 0.15°C/sec. Each reaction consisted of three parallel experiments. RNase-free ddH_2O was used as a no-template control, and human glyceraldehyde-3-phosphate dehydrogenase (GAPDH) was used to quantify the relative expression of genes. *CDKN1A, CDKN2A*, and *GAPDH* primers were used as previously described [38, 44]. The primers used are shown in Supplementary Table S2.

2.26 | Chemical compounds

Equal volumes of DMSO (D8371, Solarbio) and ATR/Atr inhibitors (ATRis/Atris), including VE-821 (HY-14731, MedChemExpress), VE-822 (S7102, Selleck, Houston, TX, USA), and ceralasertib (HY-19323, MedChemExpress), were added to LNCaP, PC-3, TRAMP-C1 and RM1 cells combined with (RT-resistant) or without (Control) radiotherapy. The ATRis were diluted to 10 mmol/L with DMSO and applied to approximately 5×10^5 cells at the following doses: VE-821, 5 μmol/L; VE-822, 300 nmol/L; and

ceralasertib, 1 μmol/L. For the animal experiments, the recipient dose was 50 mg/kg.

2.27 | Plasmids and mutagenesis

Myc-tagged murine *Cd86* and human *CD86*, as well as *Flag*-tagged murine *March1* and human *MARCH1* were constructed by subcloning the respective cDNAs into the pcDNA3.1(+)-backbone-*Myc* or pcDNA3.1(+)-*Flag* vector with the T7 promoter by Yeasen Company. The cDNA fragments were amplified by Phusion polymerase (M0530S, New England Biolabs, Ipswich, MA, USA) using Phusion High-Fidelity PCR Master Mix (M0531S, New England Biolabs).

The pLKO.1(+) plasmids encoding non-specific shRNAs (shCtr), human *ATR* shRNAs (TRCN0000039613 and TRCN0000039616) and mouse *Atr* shRNAs (TRCN0000023909 and TRCN0000023912) were purchased from Sigma-Aldrich. Human *NUP93* shRNA pools, *NUP160* shRNA pools, single-guide RNA (sgRNA) of human *MARCH1* and sgRNA of murine *March1* were purchased from Yeasen company.

The fragments, deletion, and points mutagenesis were oligonucleotide synthesis, purified using High Pressure Liquid Chromatography (HPLC), and subcloned into pcDNA3.1-*Flag*/*Myc* plasmids by Yeasen company.

The sequences of the cloning primers, including restriction enzyme sites, are provided in the Supplementary Table S2.

2.28 | Clustered regularly interspaced short palindromic repeat (CRISPR)-Cas9 system

The sgRNAs were synthesized by Yeasen Company and cloned into the LentiCRISPRv2 plasmid (52961, Addgene, Watertown, MA, USA) as previously described [44]. Briefly, an equal volume of upstream and downstream primers of sgRNA (100μmol/L) were mixed and annealed by a water bath at 95°C for 10 min, followed by natural cooling. The LentiCRISPRv2 plasmid was linearized by BsmBI enzyme (15203ES80, Yeasen) under the following reaction conditions: 55°C, 1 h; 80°C, 20 min; maintained at 4°C. The enzymatic digestion system was 0.5 μg LentiCRISPRv2 plasmid, 0.5μL BsmBI enzyme, 2.5 μL of 10 × BsmBI Buffer, and ddH_2O, for a total of 25 μL reaction system. Enzymatic products were recovered by TIANgel Midi Purification Kit (DP209, Tiangen, Beijing, China) following the manufacturer's instructions. The linearized LentiCRISPRv2 plasmid and annealed sgRNA products were subjected to ligation using T4 DNA ligase (2011A, Takara Bio) at 37°C for 4 h, followed by incubation at 4°C for maintenance. The ligation reaction was performed using a 10 μL system comprising 25 ng of linearized LentiCRISPRv2 plasmid, 2.5 μL of annealed sgRNA product, 0.2 μL of T4 DNA ligase enzyme, 1 μL of T4 DNA ligase buffer, and ddH_2O to complete the volume. Recombinant plasmids were transformed into DH5α competent cells (9057, Takara Bio) and individual positive clones were identified by Sanger sequencing (Sangon Biotech, Beijing, China).

2.29 | RNA interference

Small interfering RNA (siRNA) of *CHEK1* (SASI_Hs01_00027316, and SASI_Hs02_00331483) and negative control (SIC002) were purchased from Sigma-Aldrich. LNCaP cells were plated one day in advance to ensure 70% confluence the next day. The siRNAs were transfected into LNCaP using Lipofectamine RNAiMAX (13778030, Thermo Fisher Scientific). The transfection reagents were replaced with a complete medium after 6 h of incubation. Then, the LNCaP cells were collected and assayed 48 h after transfection. Sequence of siRNAs are listed in Supplementary Table S2.

2.30 | Transient transfection

The pcDNA3.1 plasmids were transient transfected into TRAMP-C1 and LNCaP cells with Lipofectamine 3000 (L3000015, Thermo Fisher Scientific). In short, the cells were seeded at a density of 2×10^4 cells/cm^2 in a 10 cm dish and allowed to reach approximately 70% confluence prior to transfection. A total of 15 μg of plasmid DNA was complexed with 30 μL of P3000 reagent and 45 μL of Lipofectamine 3000, following the manufacturer's protocol. The medium was replaced with fresh complete medium 6 h post-transfection. The cells were then collected 48 h after transfection and utilized for subsequent assays.

2.31 | Stable transfection

The pEXQV/pVSV-G/pLKO.1 and psPAX2/pMD2.G/LentiCRISPRv2 systems were used to format lentiviruses. In general, HEK293 cells were seeded in a 10 cm dish at a density of 5×10^4 cells/cm^2 at 24 h before transfection. On the day of transfection, the culture medium was replaced with DMEM lacking FBS. Plasmids were mixed in Opti-MEM (31985062, Thermo Fisher Scientific) and co-transfected to HEK293 cells using Lipofectamine 3000 according to the manufacturer's protocol. The medium was replaced with DMEM containing

10% FBS and sodium Pyruvate (C0331, Beyotime) at 24 h post-transfection. Viral supernatants were collected at the following 48 h and 72 h. The freshly collected viral supernatants were filtered through a 0.45 μm membrane and stored at -80°C for subsequent use.

LNCaP and TRAMP-C1 cells were seeded at a density of 2×10^4 cells/cm^2 before infection. For infection, the cell culture medium was replaced with 8 mL of complete medium and 8 mL of the filtered viral supernatant, supplemented with 12 μg/mL of polybrene (40804ES76, Yeasen). After 48 h of infection, the cells were selected with 1 μg/mL of Puromycin (A1113802, Sigma-Aldrich) for 3-5 days.

2.32 | GST-tagged recombinant protein purification and pull-down of in vitro transcribed proteins

GST-MARCH1 recombinant plasmids encoding different portions of *MARCH1* were expressed in *Escherichia coli* (BL21 competent cell) (9126, Takara Bio) and purified with glutathione Sepharose 4B beads (GE Healthcare) (17075601, Cytiva, Marlborough, MA, USA). Full-length *Myc-CD86* was cloned and inserted into the pcDNA3.1 vector with the T7 promoter. Plasmids were linearized by digestion with Xba I (R0145T, New England Biolabs) followed by purification with a TNT quick coupled transcription/translation system kit (L1170, Promega, Madison, WI, USA), and a total of 200 ng of linearized plasmid DNA was transcribed in vitro using T7 RNA polymerase (M0251S, New England Biolabs) and purified with Myc-tag beads (88842, Thermo Fisher Scientific). Purified GST-tagged recombinant proteins (2 μg) were incubated with in vitro transcribed Myc-CD86 proteins (2 μg) in NT2 buffer [50 mmol/L Tris (pH 7.4), 150 mmol/L NaCl, 1 mmol/L $MgCl_2$, 0.05% NP-40, 1 mmol/L DTT, 1 × PIC]. The ATR proteins were purified with ATR antibodies and Protein A/G beads (88802, Thermo Fisher Scientific) from LNCaP cell lysates. The mixture was incubated with ATR beads and 2 mmol/L ATP at 37°C for 30 min and then at 4°C overnight. On the second day, after five washes with PBS, the proteins were detected by Western blotting.

2.33 | Co-immunoprecipitation (Co-IP)

Freshly digested cells were lysed with IP buffer (50 mmol/L Tris-HCl (pH 7.4), 150 mmol/L NaCl, 1% NP-40, 1% sodium deoxycholate, and a 1% protease inhibitor cocktail) on ice for more than 30 min. Phosphatase λ (PPλ) (P0753S, New England Biolabs) at a concentration of 100 units/mL was used to prevent protein phosphorylation. Bafilomycin A1 (Baf-A1) (HY-100558, MedChemExpress) at a working concentration of 1 μmol/L was used to inhibit ubiquitination. The application of PPγ or Baf-A1 depended on the experimental design. Then, the cell lysate was centrifuged at 14,000 × g at 4°C for 15 min. The supernatant was collected and incubated with primary antibodies and Protein A/G agarose beads. The antibodies were diluted according to the instructions. Proteins and antibodies were incubated at 4°C overnight. The beads were washed with IP buffer 6 times and then boiled for Western blotting analysis, as previously described [45].

2.34 | Prediction of post-translational modification (PTM)

The software GPS 6.0 (https://gps.biocuckoo.cn), which integrates 30043 known site-specific kinase–substrate relationships in 7041 proteins and 22 public resources, was used for the ATR phosphorylation site prediction. The FASTA-formatted sequences of the CD86 (Gene ID: 942; Ensembl: ENSG00000114013) and Cd86 (Gene ID: 12524; Ensembl: ENSMUSG00000022901) were input into the screen of the "WEB SERVER" website, and the predicted phosphorylation sites were subsequently obtained.

2.35 | Conserved region detection

We predicted conserved regions in peptides using InterPro (http://www.ebi.ac.uk/interpro/), an online peptide conserved region prediction website. The peptide sequences of MARCH1 from human (Entry: Q8TCQ1), mouse (Entry: D3YVY0), rat (Entry: D4A6K8), dog (Entry: A0A8C0NY50), chicken (Entry: A0A8V0Y382), and African clawed frog (Entry: A0A974I0L6) were downloaded from UniProt (https://www.uniprot.org/) and submitted to InterPro. We divided peptides based on protein structure and functional regions and performed sequence comparisons via BLAST to identify conserved peptides.

2.36 | Immunofluorescence (IF) staining

IF experiments were performed as previously described [46] with modifications. Briefly, LNCaP and TRAMP-C1 cells were fixed with 4% paraformaldehyde for 10 min. After three washes with PBS, the fixed cells were permeabilized with 0.1% Triton X-100 for 20 min, washed with PBS, and then blocked with PBS supplemented with 5% BSA. The cells were incubated with the primary antibody p-ATR-T1989 (dilution 1:250; ab289363, Abcam) at 4°C overnight. After three washes with PBS, the cells were

incubated with a secondary antibody conjugated with the Alexa Fluor 594 dye (48934, Cell Signaling Technology) for 30 min at room temperature. After three washes with PBS, the cells were counterstained with Vectashield (H-1200, Vector Laboratories, Newark, CA, USA) containing 4',6-diamidino-2-phenylindole (DAPI). Images were captured using the EVOS FL AUTO 2 system (Thermo Fisher Scientific) and analyzed with ImageJ software (https://imagej.net/ij/).

2.37 | T-cell isolation and activation

T cells were isolated using previously reported methods [47]. Briefly, fresh lymphocytes were flushed from the spleens of 6-week-old C57BL/6 male WT mice with PBS and purified using a lymphocyte isolation kit (P8860, Solarbio). T cells were expanded in a 15 mL centrifuge tube with RPMI 1640 medium containing 10% FBS and 150 U/mL Il-2 (HY-P7077, MedChemExpress) for 24 h. Then, the T cells were subjected to isotype antigen stimulation twice every 7 days before being used. The day before antigen stimulation, IFN-γ (HY-P7071, MedChemExpress) at a concentration of 200 ng/mL was added to cultured tumor cells to enhance antigen presentation, and a 96-well plate was prepared by adding 5 μg/mL anti-mouse Cd28 antibody (clone: 37.51; HY-P99123, MedChemExpress) to the wells. On the day of co-stimulation, a total of 2×10^5 T cells and 1×10^4 tumor cells were added to the wells supplemented with 150 U/mL Il-2 and 20 μg/mL anti-mouse Pd-1 (clone: RMP1-14; A2122, Selleck). The medium of stimulated T cells was replaced with RPMI 1640 medium (10% FBS, 150 U/mL Il-2, and 20 μg/ml anti-mouse Pd-1) or cells were subjected to 1:1 passaging after 2 days of co-stimulation. The T cells derived from the mice were used for analysis after 14 days of culture.

2.38 | Tumor responsiveness assessment

The proportion of $Cd8^+$ T cells and the degree of tumor cell apoptosis were analyzed to assess tumor responsiveness.

For the $Cd8^+$ T-cell viability assay, a total of 1×10^5 T cells and 2.5×10^3 tumor cells were seeded in a 96-well plate precoated with the anti-mouse Cd28 antibody and cultured in RPMI 1640 medium supplemented with 10% FBS, 50 ng/mL PMA and 1 μg/mL ionomycin (2030421; Dakewe Bioengineering, Shenzhen, Guangzhou, China). T cells were collected for assays after 24 h of coculture. The proportion of $Cd8^+$ cells among the total number of $Cd3^+$ cells was analyzed.

For the tumor apoptosis analysis, the T cells were stained red with CellTracker Red CMTPX (40717ES50, Yeasen). The live cells were indicated by negative Caspase 3 expression. Briefly, a total of 1×10^4 prestained T cells and 2.5×10^3 tumor cells were seeded in a 96-well plate precoated with the anti-mouse Cd28 antibody and cultured in RPMI 1640 medium supplemented with 10% FBS and 0.1 μmol/L SuperView™ 488 Caspase-3 substrate (40273ES25, Yeasen). The cells were collected after 2 days of culture and incubated with a Percp/Cyanine5.5-conjugated Cd326 antibody (clone: G8.8; 118219, Biolegend). The $Cd326^+$ and Caspase 3^- cells were considered live tumor cells.

2.39 | Statistical analysis

GraphPad Prism 8 and R software were used for statistical analyses, with a minimum cutoff of $P < 0.05$. All the data are presented as the means ± standard deviations (SDs). Unpaired Student's t test was used to compare data with a normal distribution between two groups. The log-rank test was used for the Kaplan–Meier plot of the patient cohort. Data with a non-normal distribution were analyzed using the Mann–Whitney test. All in vivo experiments were replicated at least three times. Animal experiments were performed randomly, with at least $n = 6$ per group. $P < 0.05$ was considered statistically significant.

3 | RESULTS

3.1 | RT-resistant PCa cells were insensitive to Ctla-4 antibody treatment

We performed a GO analysis on the transcriptomic profiles of TCGA-PRAD cohort to understand the gain- and loss-of-function of RT-resistant PCa. The GO analysis revealed that T-cell activation, immune effector processes, and lymphocyte-mediated immunity were among the top 20 significantly downregulated pathways in RT-resistant PCa patients of TCGA-PRAD cohort, compared with the RT-sensitive group (all $P < 0.001$, Figure 1A). Among the RT-resistant related immune genes obtained from the GO list (Supplementary Table S3), the T cell activation-associated genes were notably implicated. The Kaplan-Meier survival analysis of the 142 samples from the RT-resistant group of the Second Hospital of Tianjin Medical University cohort revealed that the upregulation of $CD8^+$ T cell infiltration was associated with longer post-RT biochemical recurrence-free survival ($P < 0.01$, Figure 1B, Supplementary Figure S1A). However, survival in the RT-sensitive group was not associated with $CD8^+$ T-cell infiltration (Supplementary Figure S1B). These findings imply that the suppression of immune pathways could be a radiotherapy-induced characteristic of PCa that does not respond to radiotherapy.

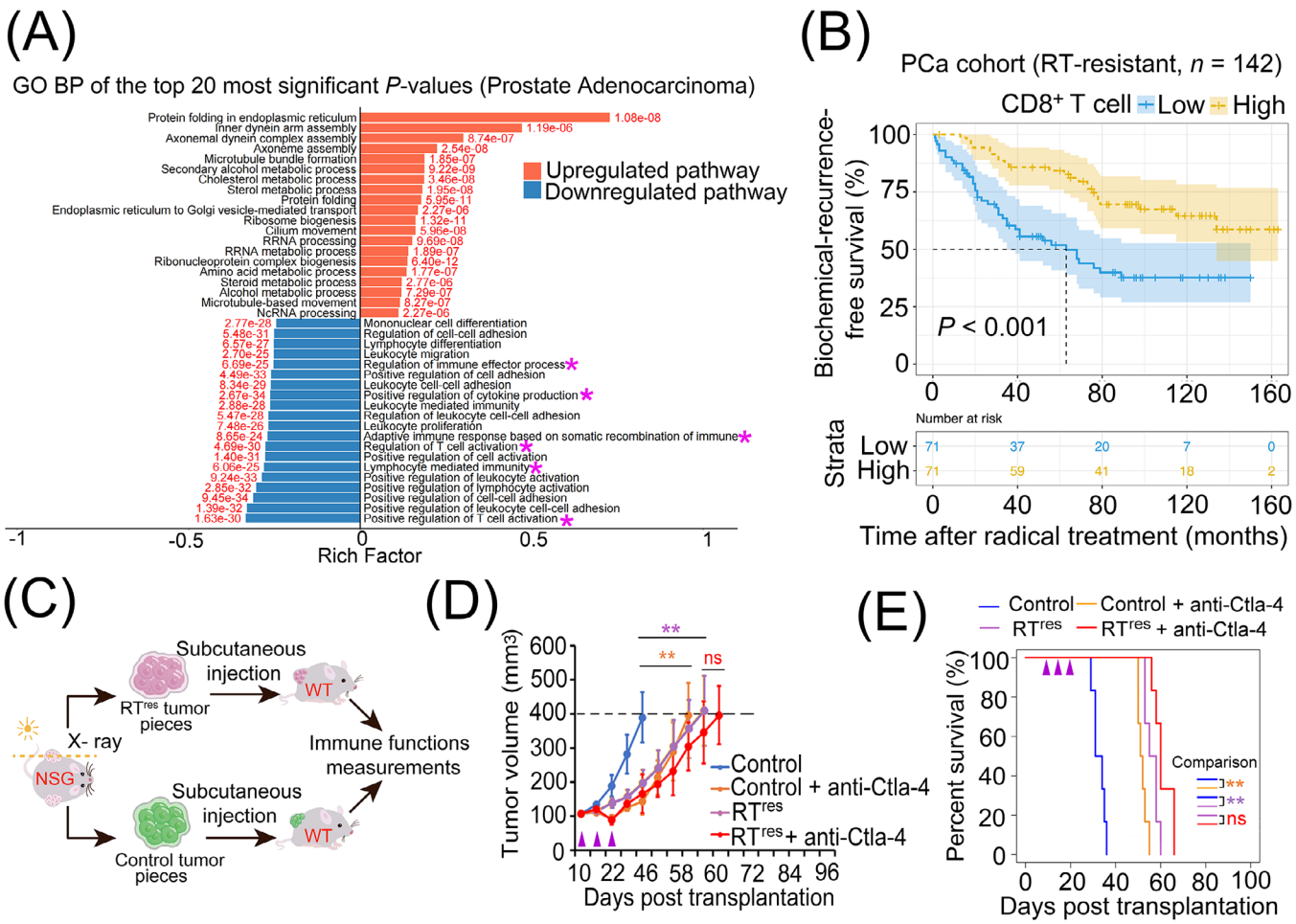

FIGURE 1 **Cancer cell senescence is associated with resistance to immunotherapy**. (A) Gene Ontology biological process (GO BP) analysis of RT-resistant PCa ($n = 15$) vs. RT-sensitive PCa ($n = 39$) from TCGA-PRAD dataset. The top 20 pathways with the lowest P values are shown for the upregulated (up) and downregulated (down) groups (Fisher's exact test). Purple asterisks indicate immune-related pathways. P value < 0.05 was considered statistically significant. (B) Kaplan–Meier plot showing biochemical-recurrence-free survival of patients with high and low level of $CD8^+$ T cell infiltration in the RT-resistant PCa cohort of the Second Hospital of Tianjin Medical University. Patients were divided based on the medium CD8 expression levels ($n = 71$ for each group). (C) Schematic representation of the experimental strategy for measuring immune function in cells stimulated with RT in vivo. TRAMP-C1 cells were implanted subcutaneously into both sides of 6-week-old NSG male mice. RT-resistant tumors were generated using unilateral ionizing radiation (X-ray, 10 Gy) and are shown in rose red. Untreated tumor cells served as controls and are shown in green. The control and RT-resistant tumor cells were injected into the flanks of 6-week-old male C57BL/6 WT mice to eliminate the immune response to anti-Ctla-4 antibody treatment. Anti-Ctla-4 treatment and immune function measurements were performed as described above. (D) Tumor volume analysis of control, control + anti-Ctla-4, RT-resistant, and RT-resistant + anti-Ctla-4 tumors in WT C57BL/6 mice ($n = 6$ for each group). The control group of mice received an equivalent concentration of the IgG2a isotype control antibody. The purple triangle indicates the anti-Ctla-4 injection. The data are presented as the means ± SDs. The tumor volume curves were statistically analyzed via two-sided Student's t tests. (E) Survival analysis of control, control + anti-Ctla-4, RT-resistant, and RT-resistant + anti-Ctla-4 tumors in WT C57BL/6 mice ($n = 6$ for each group). The control group of mice received an equivalent concentration of the IgG2a isotype control antibody. Survival curves were analyzed using the log-rank test. * $P < 0.05$, ** $P < 0.01$, *** $P < 0.001$, and ns, not significant. Abbreviations: GO BP, Gene Ontology biological process; NSG, NOD.Cg-Prkdc^{scid}Il2rg^{Tm1Wjl}/SzJ; PCa, prostate cancer; RT, radiotherapy; RT^{res}, radiotherapy resistant; SD, standard deviation; TCGA, The Cancer Genome Atlas; PRAD; WT, wild-type.

We generated TRAMP-C1 tumors in immunodeficient NSG mice to test whether the RT-related pathway sensitized tumors to antitumor immunotherapy. Both tumors located on opposite sides of the same animal, with the same volume, were subjected to treatment with or without radiation to induce the development of RT-resistant tumors. The tumor volumes of the two groups were very similar (Supplementary Figure S1C-D). Next, we tested the antitumor immunity of the implanted tumors (Figure 1C). RT-resistant tumors implanted in WT mice exhibited slow

growth and did not respond to treatment with anti-Ctla-4 antibodies, in contrast to the control tumors, which were sensitive to this antibody treatment (Figure 1D). The survival data revealed that the RT-resistant group had slightly prolonged survival but didn't sensitive to immunotherapy (Figure 1E). In addition, we observed a decrease in the expression of CD86 in RT-resistant PCa cells, but the expression of MHC I and MHC II remained unchanged (Supplementary Figure S1E-F). Thus, these findings suggest that Ctla-4 antibody treatment does not confer any additional antitumor immunity benefits to RT-resistant PCa cells in the transplantable tumor model.

3.2 | RT-resistant PCa cells exhibited senescent features and ATR activation

Given the diminished immune response in RT-resistant PCa, we investigated the underlying genetic factors associated with these cells. The cellular diversity of PCa cells was profiled by scRNA-seq to characterize the temporal dynamics of PCa cells under RT stress. scRNA-seq of unirradiated LNCaP cells and RT-resistant LNCaP cells revealed different cellular properties (Figure 2A-B). Cluster 4, 6, and 9 were RT-resistant cell clusters exhibiting a loss of immune pathways (Figure 2C). A senescent pathway was found in Cluster 4 and 6 (Supplementary Figure S2A). Moreover, our data indicated that more than 50% of RT-resistant PCa cells were positive for β-Gal (Supplementary Figure S2B). However, we still found that approximately 40% of RT-resistant PCa cells activated cell division and proliferation pathways (Supplementary Figure S2C), suggesting that RT-resistant cells survived and replicated. A pseudotime analysis of the cells using Monocle 2 suggested two diverging cell fates, starting at Cluster 7 (only in the control group), progressing toward Cluster 0 at one end and Cluster 3, 5 and 8 at the other end, with Cluster 4, 6, and 9 indicating an intermediate state and spreading along the axis (Figure 2D-E). One end of the pseudotime trajectory was characterized by cell proliferation events, such as routes involved in chromosomal segregation, nuclear division, and the cell cycle. The other end of the pseudotime trajectory was marked by cell development events with nervous system development related pathways activated (Figure 2E and Supplementary Figure S2D), which were consistent with the clinical PCa tumor progression data [48, 49]. However, the pseudotime analysis revealed an intriguing intermediate state in which PCa senescence occurred as a result of RT stress. The KEGG analysis revealed that the DNA replication pathway was present in Clusters 4 and 6 (Supplementary Figure S2A), which were unique to RT resistant. *ATR* is one of the most important genes upstream of DNA replication signaling [50, 51]. Interestingly, we detected a similar early-to-late trajectory of *ATR* with the senescence marker genes *CDKN1A* and *CDKN2A* [38, 52] (Figure 2F and Supplementary Figure S2E), suggesting that these clusters highly expressed the *ATR* gene along with senescence markers. The gene distribution analysis revealed that *ATR* levels were positively associated with *CDKN1A/CDKN2A* expression and negatively associated with the RNA levels of *PARP1* and *PRKDC* (encoding DNAPKcs) in RT-resistant specific Clusters 4 and 6 (Figure 2G). However, there was no change in the expression of *CD80* and *CD86* was observed in the clusters (Supplementary Figure S2F), indicating that senescence does not affect the B7 family at the RNA level. Precomputed data from the xCell website revealed an interesting finding: patients with higher *ATR* expression had a highly immunosuppressive tumor microenvironment consisting of a low proportion of $CD8^+$ naïve T cells and T helper type 1 (Th1) cells, as well as an abundance of T regulatory (Treg) cells (Supplementary Figure S2G), which was consistent with T-cell infiltration in PCa tumors [48]. In vitro coculture experiments revealed that senescent PCa cells were involved in immune escape (Supplementary Figure S2H). These findings imply a substantial association between RT-resistant PCa cells and immunological responses. Thus, the data indicated that specific subgroups within the RT-resistant population presented senescence-associated traits, notably with elevated expression of ATR. In terms of molecular mechanisms, ATR appears to be significant factor linking cellular senescence to T-cell-mediated immune responses.

3.3 | The senescence-related protein ATR negatively regulated CD86 expression at the protein level

We assessed the ATR protein levels in FFPE tissues matched with RNA data to thoroughly investigate the relationships between ATR expression, immunological processes, and senescence. The samples characterized by high expression of both *CDKN1A* and *CDKN2A* ($CDKN1A^{high}CDKN2A^{high}$) were considered as senescent tissue samples (Supplementary Figure S3A). Senescent tissues were verified by the expression of the canonical senescence-associated secretory phenotype (SASP) factors *IL-6, IL-8, SPINK1, SFRPS*, and *MMP3* (Supplementary Figure S3B). Consistent with the scRNA-seq data, $CDKN1A^{high}CDKN2A^{high}$ clinical senescent tissues presented a higher level of ATR staining than $CDKN1A^{low}CDKN2A^{low}$ tissues (Figure 3A). The IHC analysis revealed that approximately 70% of $CDKN1A^{high}CDKN2A^{high}$ tumors exhibited strong or

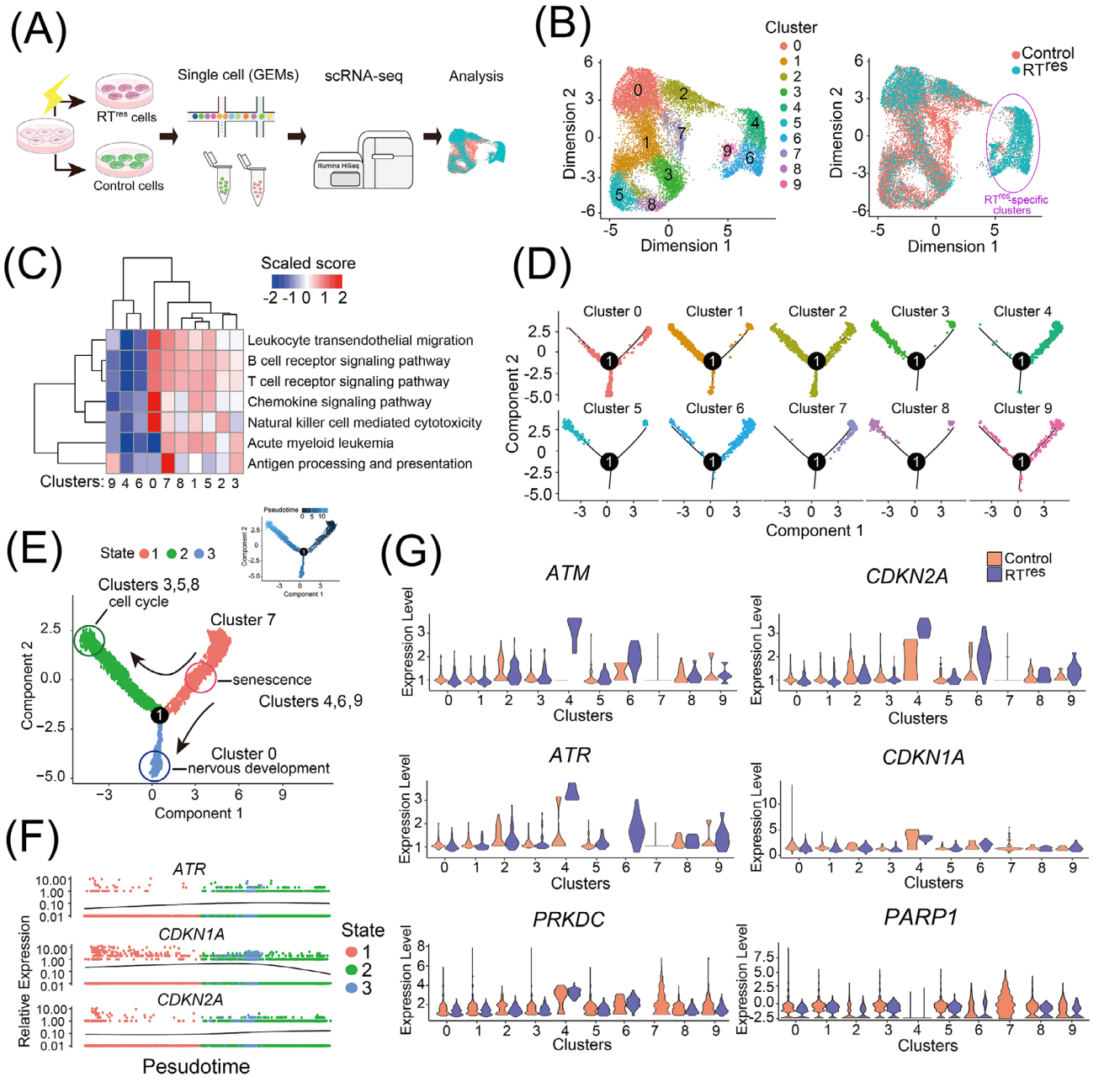

FIGURE 2 **scRNA-seq analysis of cancer cell senescence**. (A) Schematic diagram of scRNA-seq of LNCaP RT-resistant cells. The cells treated with (RT-resistant cells, rose red) or without (control cells, green) radiation were analyzed via scRNA-seq. (B) UMAP analysis of 16,664 single cells, color-coded by clusters (left) and group (right). The control group and the RT-resistant group shared the same clusters (Cluster 1, 2, 3, 5, and 8). Cluster 7 was unique to the control group. Clusters 4, 6, and 9 were the main components of the RT-induced senescence group. (C) Heatmap of the enrichment of immune-related gene sets in each cluster according to GSVA. Differences in pathway activities were scored for each cluster using GSVA, and Cluster 4, 6, and 9 (columns) presented lower scores for immune-related pathways (rows) than the other clusters did. The GSVA score represents the absolute enrichment of the gene set in each sample. (D) Pseudotime trajectories of cells of each cluster analyzed by Monocle 2. (E) Randomly, 10,000 cells are ordered along pseudotime trajectories, and the cells differentiate into two fates from the prebranch, with the cells color-coded by cluster. (F) Kinetic plots showing the associations between senescence-related gene expression and trajectory states. The expression levels of *ATR, CDKN1A*, and *CDKN2A* were arrayed along the pseudotime trajectory, whereas the expression levels of *CDKN1A* increased at state 1 and decreased at state 2. (G) The expression of the *ATM, ATR, CDKN2A, CDKN1A*, *PARP1*, and *PRKDC* genes in each cluster and group is shown in the violin plot. Compared with the control group, the senescence groups expressed higher levels of related genes in Cluster 4 and 6. Abbreviations: ATM, ataxia telangiectasia mutated; ATR, ataxia telangiectasia and Rad3-related protein; CDKN1A, cyclin-dependent kinase inhibitor 1A; CDKN2A, cyclin-dependent kinase inhibitor 2A; GSVA, gene set variation analysis; PARP1, poly (ADP–ribose) polymerase 1; PRKDC, Protein Kinase C Delta; RT^{res}, radiotherapy-resistant; scRNA-seq, single-cell RNA sequencing; UMAP, uniform manifold approximation and projection.

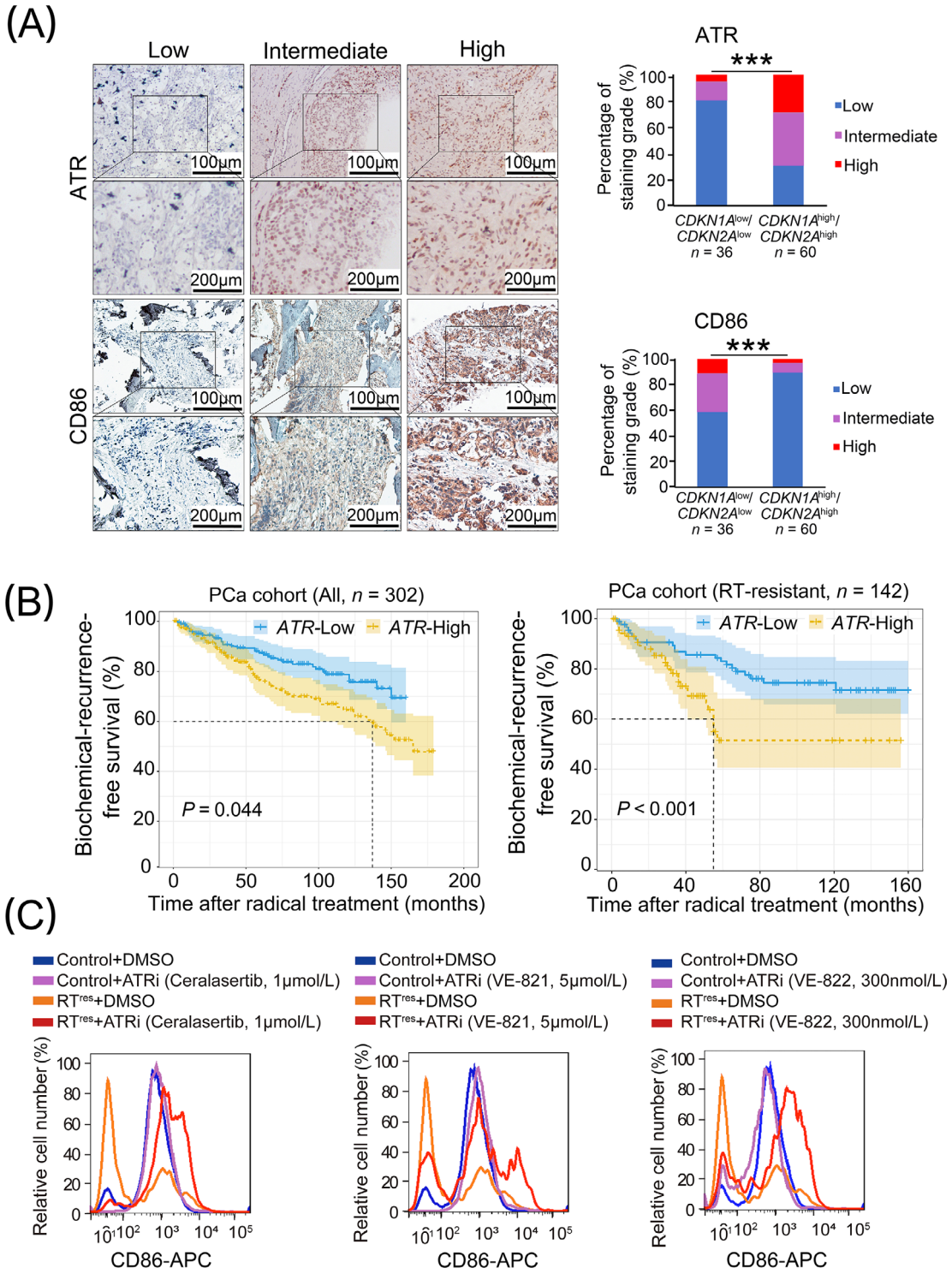

FIGURE 3 **ATR and CD86 protein levels in clinical samples**. (A) Total ATR and CD86 IHC staining results from 96 patients with RT-resistant PCa. Left panel, representative images of ATR and CD86 staining grade; right panel, quantitative data for the total percentage of ATR and CD86 protein staining. Statistical significance was determined by the Wilcoxon rank-sum test. *** $P < 0.001$. (B) Kaplan–Meier survival analysis of the relationship between the level of *ATR* and biochemical-recurrence-free survival time of PCa patients from the Second Hospital of Tianjin Medical University cohort. The left panel shows the analysis of all samples ($n = 151$ per group), and the right panel shows the analysis of the RT-resistant samples ($n = 71$ per group). *P* values are shown in the figures. (C) FACS analysis of the surface expression of CD86 following ATR inhibition by ceralasertib, VE-821, or VE-822 in RT-resistant PCa cells. After 48 h of inhibitor treatment, a flow cytometry analysis was performed from three independent experiments. Abbreviations: ATR, ataxia telangiectasia and Rad3-related protein; CDKN1A, cyclin-dependent kinase inhibitor 1A; CDKN2A, cyclin-dependent kinase inhibitor 2A; IHC, immunohistochemistry; PCa, prostate cancer; RT^{res}, radiotherapy-resistant.

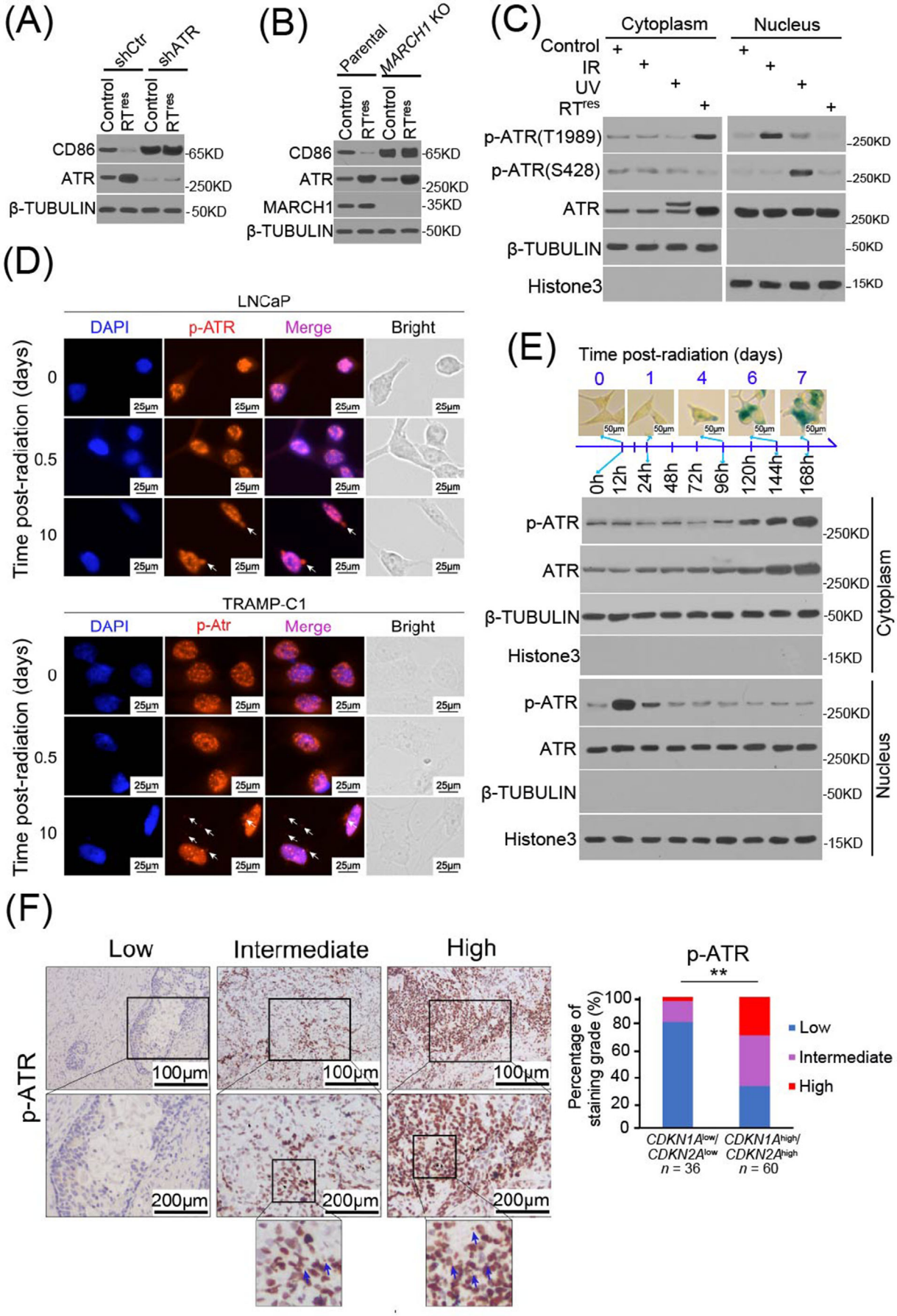

intermediate staining for ATR but that approximately 15% of the tumors exhibited staining for CD86 (Figure 3A). CD80 was undetectable in PCa tissues (Supplementary Figure S3C). The patient survival data indicated that higher *ATR* expression was associated with shorter biochemical-recurrence-free survival in PCa patients in our post-RT cohort (Figure 3B) and in TCGA cohort (Supplementary Figure S3D). Another DNA repair gene, *ATM*, was not associated with DFS survival or the expression of senescence markers (Supplementary Figure S3E-F), suggesting that ATR may be a senescence-related protein without a DNA repair function in PCa. Similarly, equivalent RNA levels of *CD86* were detected in control and RT-resistant cells (Supplementary Figure S3G), suggesting that senescence mediated CD86 expression at the protein level through ATR activation. An analysis of CD86 expression on the surface of the membrane revealed a significant reduction in the LNCaP RT-resistant group, whereas this decrease was reversed by ATRis, leading to the restoration of CD86 expression on the surface (Figure 3C and Supplementary Figure S3H-I). We conducted in vitro coculture experiments of T cells with tumor cells derived from TRAMP-C1 and RM1 lines to assess how T cells respond to tumors with low Cd86 expression and the effects of Atris. The data revealed that the overexpression of Cd86 promoted the killing of PCa cells by T cells (Supplementary Figure S3J-K). Atris enhanced the capacity of T cells to kill tumor cells and increased the proportion of $CD8^+$ T cells among the total T cells (Supplementary Figure S3L-N). These results demonstrated that senescence mediated CD86 protein expression through ATR.

3.4 | Senescence released cytosolic ATR

Next, we sought to understand the molecular mechanism by which ATR mediates the production of CD86, a key ligand of CTLA-4. Knockdown of *ATR* increased CD86 protein levels but did not affect CD80 levels (Supplementary Figure S4A). We also found that the depletion of ATR rescued the protein levels of CD86 in RT-resistant PCa cells (Figure 4A). Notably, CHK1, the downstream target of ATR, plays a role in activating apoptosis to kill cells or triggering DNA repair [53]. However, in this study, we ruled out the possibility that ATR might phosphorylate CD86 through CHK1 (Supplementary Figure S4B). Interestingly, CD86 ubiquitination was increased by Baf-A1 in RT-resistant PCa cells (Supplementary Figure S4C), suggesting that CD86 is involved in endosome recycling. CD86 degradation may involve MARCH1-mediated ubiquitination [54, 55]. Knocking out *MARCH1* rescued the protein level of CD86 in RT-resistant PCa cells (Figure 4B and Supplementary Figure S4D). Ubiquitination assays revealed that senescence increased the ubiquitination of CD86 in LNCaP cells that were resistant to RT. Conversely, the suppression of ATR activity mitigated this increase in ubiquitination (Supplementary Figure S4E). A previous study showed that ATR functions as a cytosolic protein to regulate ultraviolet-induced apoptosis [56]. As CD86 is a protein found in the cell membrane, we investigated whether ATR directly affects CD86 levels in the cytoplasm. The results of the cell fractionation assays revealed that the ATR protein was expressed in both the nucleus and cytoplasm of PCa cells (Figure 4C-D). Additionally, T1989 site-phosphorylated ATR (p-ATR) was activated in the

FIGURE 4 **ATR downregulated CD86 expression in PCa cells**. (A) Western blotting revealed that ATR was knocked down in LNCaP parental and RT-resistant cells. The cells were infected with a nonspecific shRNA (shctr) or two independent *ATR* shRNA mixtures, and after 48 h, the cells were harvested for Western blotting. β-TUBULIN served as an internal control. (B) Cells were infected with a nontargeting sgRNA (parental) or *MARCH1* sgRNAs. The parental cells and *MARCH1*-KO cells were selected with puromycin for 2 weeks, after which the single clones were cultured and unirradiated or irradiated. The unirradiated and senescent cells were harvested for Western blotting. β-TUBULIN was used as an internal control. (C) LNCaP cells were treated with 10 Gy of radiation (acquired at 1 h post-radiation), ultraviolet (254-nm lamp at a frequency of 0.83 J/m^2/sec) or senescence (acquired at 10 days after 10 Gy radiation). The cells were lysed with different buffers to obtain fractions of the cytoplasm and nucleus. ATR and p-ATR (Thr1989) levels were determined using Western blotting. β-TUBULIN served as a cytoplasmic control; Histone 3 served as a nuclear control. (D) LNCaP and TRAMP-C1 cells were treated with the sham, 10 Gy of radiation (acquired immediately after irradiation, short-term), or senescence (acquired at 10 days after 10 Gy radiation, long-term). p-ATR (Thr1989) levels were detected using IF staining. (E) Expression levels of ATR and p-ATR(Thr1989) in LNCaP cells along with cellular senescence. LNCaP cells were treated with 10 Gy of radiation to induce senescence. β-Gal staining at days 0, 1, 4, 6, and 7 is shown. The cells were lysed with different lysis buffers at different times after irradiation to obtain fractions of the cytoplasm and nucleus. ATR and p-ATR (Thr1989) levels were detected using Western blotting. β-TUBULIN served as a cytosolic control; Histone 3 served as a nuclear control. (F) p-ATR (Thr1989) IHC staining in 96 RT-resistant PCa samples. Left panel, representative images of p-ATR IHC staining grade; right panel, quantitative data for p-ATR protein staining. Statistical significance was determined by the Wilcoxon rank-sum test. * $P < 0.05$, ** $P < 0.01$, *** $P < 0.001$, and ns, not significant. Abbreviations: β-Gal, β-galactosidase; ATR, ataxia telangiectasia and Rad3-related protein; CDKN1A, cyclin-dependent kinase inhibitor 1A; CDKN2A, cyclin-dependent kinase inhibitor 2A; IF, immunofluorescence; IHC, immunohistochemistry; IR, irradiation; KO, knockout; MARCH1, membrane-associated ring-CH-type finger 1; RT^{res}, radiotherapy resistant; sgRNA, single guide RNA; shRNA, small hairpin RNA or short hairpin RNA; UV, ultraviolet

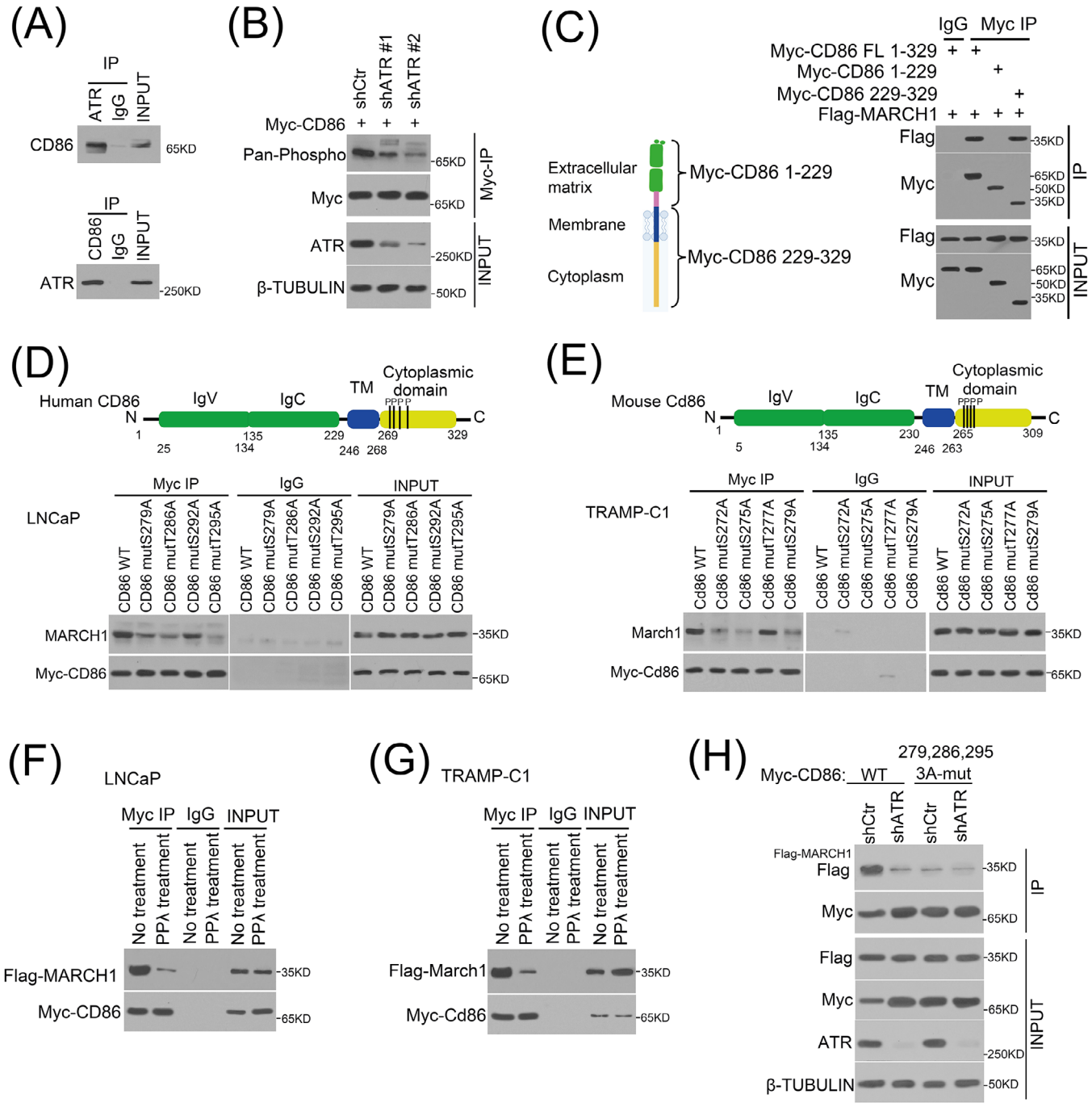

FIGURE 5 **ATR phosphorylates CD86 to increase its interaction with MARCH1 in human and mouse PCa cells**. (A) Western blots of samples from RT-resistant LNCaP cells subjected to Co-IP assays with IgG, anti-CD80, or anti-ATR antibodies. (B) Western blotting assay shows *ATR* KO in RT-resistant LNCaP cells. The cells were infected with nonspecific shRNAs (shCtr) or two independent *ATR* shRNAs, and after 48 h, the cells were harvested for Western blotting. (C) LNCaP cells were infected with *Flag-MARCH1* and *Myc-CD86* full-length or 1-229 amino acid or 229-329 amino acid, and after 48 h, the cells were harvested for IP and Western blotting. FL, full length. (D) Western blots show the human CD86 phosphorylation sites. Upper panel, a diagram shows the different domains of human CD86 and possible phosphorylation sites in CD86. Variable domain (IgV), constant domain (IgC), transmembrane domain (TM). Lower panel, Western blots of samples from the Co-IP analysis using IgG or an anti-Myc-CD86 antibody and lysates from LNCaP cells transfected with WT CD86 and point mutants. (E) Western blotting was used to identify phosphorylation sites in murine Cd86. Upper panel, a diagram shows the different domains of murine Cd86 and possible phosphorylation sites in murine Cd86. Lower panel, Western blots of samples from the Co-IP analysis using IgG or an anti-Myc-Cd86 antibody and lysates from TRAMP-C1 cells transfected with WT Cd86 and point mutants. (F) Western blots of samples subjected to Co-IP analysis with IgG, anti-Myc-CD86, and anti-Flag-MARCH1 antibodies in lysates from LNCaP cells. The cell lysate was treated with PPλ at 30°C for 30 min. (G) Western blots of TRAMP-C1 cell lysates that were subjected to Co-IP analysis with rabbit IgG,

cytoplasm through RT-induced senescence (Figure 4C-D and Supplementary Figure S4F). We found that nuclear ATR was phosphorylated at 12 h post-radiation, but both the cytosolic ATR and p-ATR levels were increased by RT-induced senescence (Figure 4E). The cytosolic location and upregulation of p-ATR were verified in human PCa tissues via IHC staining (Figure 4F). Notably, senescence opens nuclear pore complexes and releases some nuclear molecules into the cytoplasm [57, 58]. We found that the release of ATR from the cytoplasm was blocked by the absence of nuclear pore complex formation when NUP93 and NUP160 were knocked down (Supplementary Figure S4G). These data indicated that the senescence-induced cytosolic translocation of ATR induced the upregulation of CD86 in PCa cells.

3.5 | Interaction between CD86 and MARCH1 through the phosphorylation of CD86

Co-IP experiments revealed the interaction between endogenous ATR and CD86 (Figure 5A). We found that ATR bound to the CD86 cytosolic domain in LNCaP cells (Supplementary Figure S5A). Fragment deletion experiments revealed that ATR was associated with the amino acid 304-329 domain of CD86 in LNCaP cells (Supplementary Figure S5B). The panshosphorylation data revealed that ATR knockdown inhibited the panshosphorylation of CD86 (Figure 5B). We predicted the possible phosphorylation sites on CD86 using the software GPS 6.0. The PTM prediction revealed four possible ATR phosphorylation sites in the cytoplasmic domain of human CD86 and mouse Cd86 (Supplementary Figure S5C). The cytoplasmic domain and the transmembrane domain have been identified as the regions where CD86 interacts with its E3 ligase MARCH1 [54, 59]. We confirmed that MARCH1 bound to the cytoplasmic domain of CD86 (Figure 5C). To investigated the impact of ATR-induced phosphorylation on the binding of CD86 and MARCH1, we conducted site-directed mutagenesis of the phosphorylation sites in the cytoplasmic domain of CD86. The Co-IP assays and Western blotting assays showed that mutations of the phosphorylation sites S279A, T286A, or T295A partially hindered the interaction between CD86 and MARCH1, whereas the S292A mutation did not have the same effect (Figure 5D). Similarly, alterations of phosphorylation sites in the same area of mouse Cd86 also partially impeded the interaction between Cd86 and March1 in TRAMP-C1 cells (Figure 5E). The interaction between CD86 and MARCH1 was decreased by PPλ in both human and murine PCa cells (Figure 5F-G). ATR depletion reduced the interaction between wild-type CD86 and MARCH1 but did not affect the interaction with the CD86 S279A, T286A, and T295A mutants (Figure 5H).

We transcribed and translated CD86 and MARCH1 in vitro to explore whether phosphorylation has a direct or indirecteffect on the CD86-MARCH1 interaction. MARCH1 binding to CD86 was directly reliant on ATP and ATR (Supplementary Figure S6A). We also observed that CD86 bound to the C-terminal cytoplasmic domain of MARCH1 (Figure 6A). Based on the amino acids in the cytoplasmic region of MARCH1, we identified two conserved regions (RRLK and KKLEK) in the MARCH1 cytoplasmic region in different species (Figure 6B). We hypothesized that phosphorylation at specific sites on CD86, located in the cytoplasmic region, strengthens binding to the MARCH1 cytoplasmic domain through electrostatic interactions. This hypothesis was tested through experiments with targeted deletions, which revealed that the RRLK motif of CD86 significantly influences the interaction with MARCH1 (Figure 6B). Deletion or mutation of the RRLK motif impaired the interaction between CD86 and MARCH1 in human PCa cells and mouse PCa cells (Figure 6C-E). Additionally, we discovered that in both human and mouse PCa cells, the ubiquitination of CD86 was somewhat reduced by mutations of three phosphorylation sites: all mutations or RRLK deletion (Supplementary Figure S6B). Basic amino acid exchange blocked the degradation of CD86 induced by ATRis (Figure 6F and Supplementary Figure S6C). Compared with those in control tumors, RT-resistant tumors with RRLK domain-deletion implanted in WT mice were profoundly sensitized to anti-Ctla-4 antibody treatment (Figure 6G-H and Supplementary Figure S6D). Therefore, these data suggest that ATR phosphorylates CD86 to enhance the interaction between CD86 and MARCH1 (Figure 6I).

anti-Myc-Cd86, or anti-Flag-March1 antibodies. The cell lysate was treated with PPλ at 30°C for 30 min. (H) IP assay showing ATR knockdown in RT-resistant LNCaP cells. The cells were infected with nonspecific shRNA (shCtr) or two independent *ATR* shRNA mixtures along with *Myc-CD86*-WT or *Myc-CD86*-3Amut (S279A, T286A, or T295A), and after 48 h, the cells were harvested for Co-IP assays with IgG or anti-Myc-CD86. β-TUBULIN was used as an internal control. Abbreviations: ATR, ataxia telangiectasia and Rad3-related protein; FL, full length; IgC, constant domain; IgV, variable domain; IP, immunoprecipitation; KO, knock out; MARCH1, membrane-associated ring-CH-type finger 1; PPλ, phosphatase λ; RT, radiotherapy; shRNA, small hairpin RNA or short hairpin RNA; TM, transmembrane domain; WT, wild type.

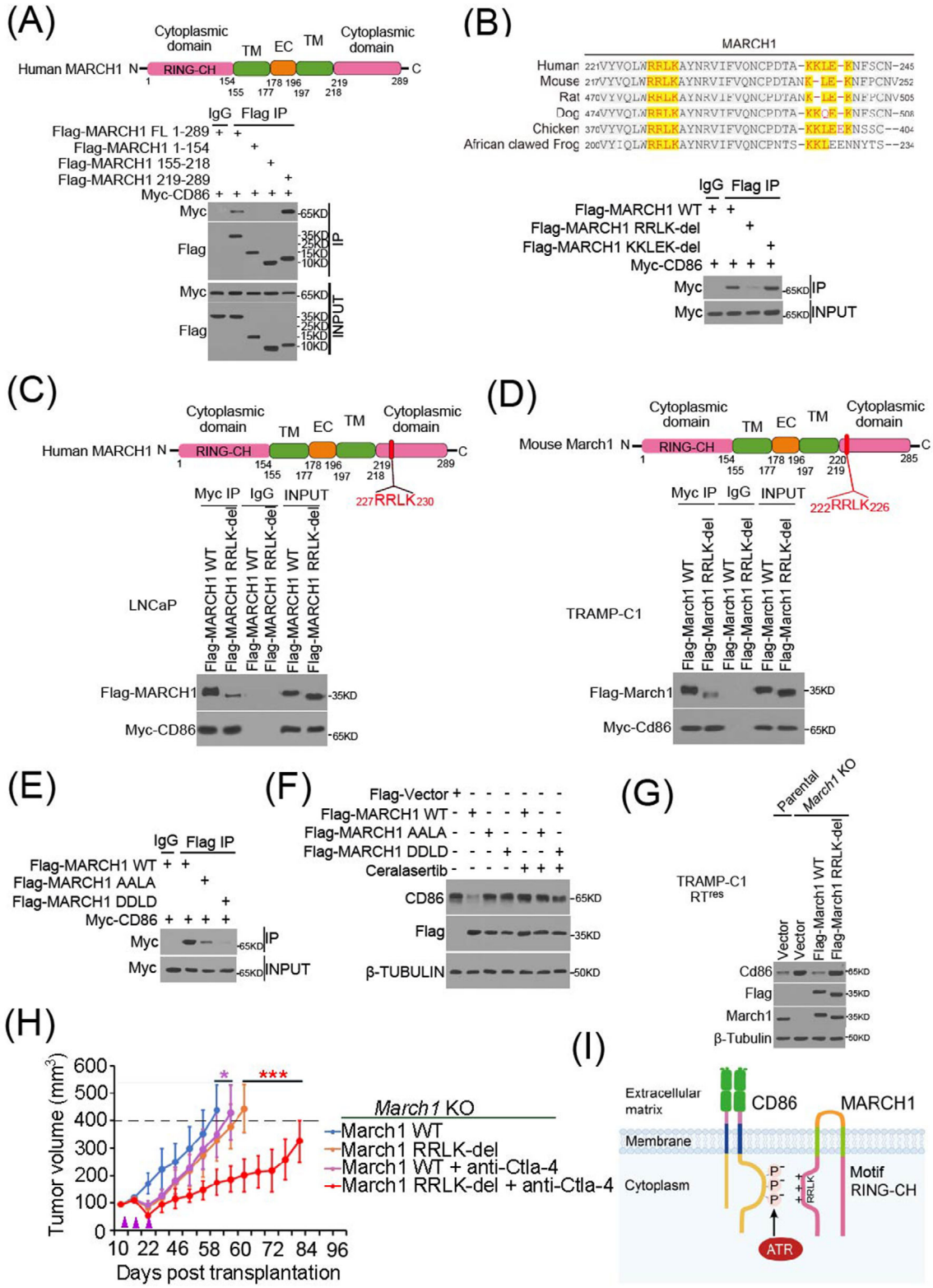

FIGURE 6 **The conserved RRLK motif is critical for the interaction of MARCH1 with CD86.** (A) LNCaP cells were infected with *Myc-CD86* and *Flag-MARCH1* full-length or 1-154 amino acid, 155-218 amino acid, or 219-289 amino acid fragments, and after 48 h, the cells were harvested for Flag IP and Western blotting. FL, full length. (B) Conserved amino acids in MARCH1 from human, mouse, rat, dog, chicken, and African clawed frog are highlighted in yellow. LNCaP cells were infected with the *Flag* empty vector, *Flag-MARCH1* WT, or *Flag-MARCH1* RRLK-deleted mutants (-del), and after 48 h, the cells were harvested for Flag IP and Western blotting. (C) Western blotting assay for the human CD86-MARCH1 binding site identification. Upper panel, a diagram showing different domains of the human MARCH1 and basic amino acids in the RRLK motif of MARCH1. Lower panel, Western blots of samples subjected to Co-IP analysis using IgG or

3.6 | The combination of ATR and Ctla-4 inhibited immune evasion

We evaluated the progression of tumors and their response to immunotherapy to assess the impact of ATR on anti-tumor immunity and cancer sensitization. Our findings indicated that, compared with control tumors, tumors with reduced Atr expression exhibited slower growth and increased sensitivity to anti-Ctla-4 antibody treatment when implanted into WT mice (Figure 7A). The survival data revealed that Atr-deficient tumors prolonged mouse survival in response to immunotherapy (Figure 7A). Cd86 expression in tumors was detected and the results suggested that the loss of Atr upregulated Cd86 protein levels in tumors (Supplementary Figure S7A). We obtained similar results in mouse tumors after ATRi treatment. A combination of a murine anti-Ctla-4 monoclonal antibody and ATRi (ceralasertib) resulted in slower tumor growth and longer survival in mice (Figure 7B). Western blotting assays revealed that ceralasertib upregulated Cd86 protein levels in tumors (Supplementary Figure S7B). The body weights of the mice were decreased after treatment with anti-Ctla-4 antibodies or ceralasertib (Supplementary Figure S7C-D). Moreover, both Atr knockdown and ATRis significantly increased the infiltration of immune effectors, including $Cd45^+Cd8^+$ T cells and $Cd45^+Cd4^+$ T cells, into RT-resistant tumors (Figure 7C). Consistent with the effects on tumor regression, cotreatment with ATR and Ctla-4 inhibitors dramatically increased $Cd45^+Cd8^+$ and $Cd45^+Cd4^+$ T-cell infiltration (Figure 7C). These data suggest that the absence of Atr leads to an increase in immune responses within senescent tumor cells (Supplementary Figure S7E).

4 | DISCUSSION

In this study, we pinpointed the pathways associated with the loss of the immune response in RT-resistant PCa, with a particular focus on intrinsic cellular factors. Our findings indicate that senescent PCa cells are resistant to immunotherapy, which is attributed to specific post-translational modifications of CD86. The modification of CD86 by cytosolic ATR enhances the binding of the E3 ubiquitin ligase MARCH1. The scRNA-seq analysis provided novel insights into senescence progression and the tumor microenvironment in PCa.

Previous studies of senescence have focused primarily on the tumor microenvironment, such as the roles of senescent $CD8^+$ T cells [60, 61] and NK cells [62]. However, the role of cancer cell senescence in cancer–immune crosstalk remains unclear. In this study, we focused on intrinsic molecules in PCa cells and tried to to figure out how PCa cells evolve after RT. Senescent cancer cells induced by radiotherapy are challenging to sample in vivo because of the small size or disappearance of metastatic cancers posttreatment, making the collection of samples for IHC staining or scRNA-seq to identify senescent subgroups difficult. We utilized a mouse model to mimic the treatment of senescent tumors with radiotherapy. The GO analysis of TCGA-PRAD cohort revealed that senescent PCa was a more common immune reaction-related cancer than RT-sensitive PCa was, which was consistent with a report that late-passage PCa cells in mice do not respond to anti-Ctla-4 antibody treatment. We further discovered that senescent tumors in WT mice did not respond to anti-Ctla-4 antibody treatment. Interestingly, the PCa senescent state was revealed by a pseudotime analysis using scRNA-seq to be

anti-Flag-MARCH1 antibodies in lysates from LNCaP cells transfected with WT *MARCH1* and *MARCH1* point mutants. (D) Western blotting assay for murine Cd86-March1 binding site identification. Upper panel, a diagram showing different domains of murine March1 and basic amino acids in the RRLK motif March1. Lower panel, Western blots of samples from the Co-IP analysis of lysates from TRAMP-C1 cells transfected with WT *March1* and point mutant *March1*. (E) LNCaP cells were infected with *Myc-CD86* and *Flag-MARCH1* WT, *Flag-MARCH1* RRLK/AALA mutants (AALA), or *Flag-MARCH1* RRLK/DDLD mutants (DDLD), and after 48 h, the cells were harvested for Flag IP and Western blotting. (F) LNCaP cells were infected with a *Flag* empty vector, *Flag-MARCH1* WT, *Flag-MARCH1* RRLK/AALA mutant (AALA), or *Flag-MARCH1* RRLK/DDLD mutant (DDLD) and treated with or without an ATR inhibitor (ATRi, ceralasertib 1 μmol/L). After 48 h, the cells were harvested for Western blotting. (G) TRAMP-C1 parental or *March1*-KO cells were infected with the *Flag* empty vector, *Flag-March1* WT, or *Flag-March1* RRLK-deleted mutant (-del), and after 48 h, the cells were harvested for Western blotting. (H) Implanted tumor volume in WT C57BL/6 mice. *March1*-KO TRAMP-C1 cells transfected with *March1*-WT or *March1*-RRLK-deletion were injected into the flanks of WT mice and administrtion with or without anti-Ctla-4 ($n = 6$ for each group). The cells in all the groups were subjected to unilateral ionizing radiation (X-ray, 10 Gy). Purple triangle, antic-Ctla-4 injection. The data are presented as the means ± SDs. Tumor volume curves were estimated by two-sided Student's t test; $^*P < 0.05$, $^{**}P < 0.01$, $^{***}P < 0.001$ and ns, not significant. (I) A diagram showing the positive–negative interaction between MARCH1 and CD86. Abbreviations: AA, amino acid; AALA, Flag-MARCH1 RRLK/AALA mutation; ATRi, ATR inhibitor; Ctla-4, cytotoxic T-lymphocyte-associated protein 4; DDLD, Flag-MARCH1 RRLK/DDLD mutation; del, deletion mutation; EC, extracellular cadherin; FL, full length; IP, immunoprecipitation; KO, knockout; MARCH1, membrane-associated ring-CH-type finger 1; ns, no significance; RING-CH, really interesting new gene-cysteine-histidine; SD, standard deviation; TM, transmembrane domain; WT, wild type; WT, wild-type.

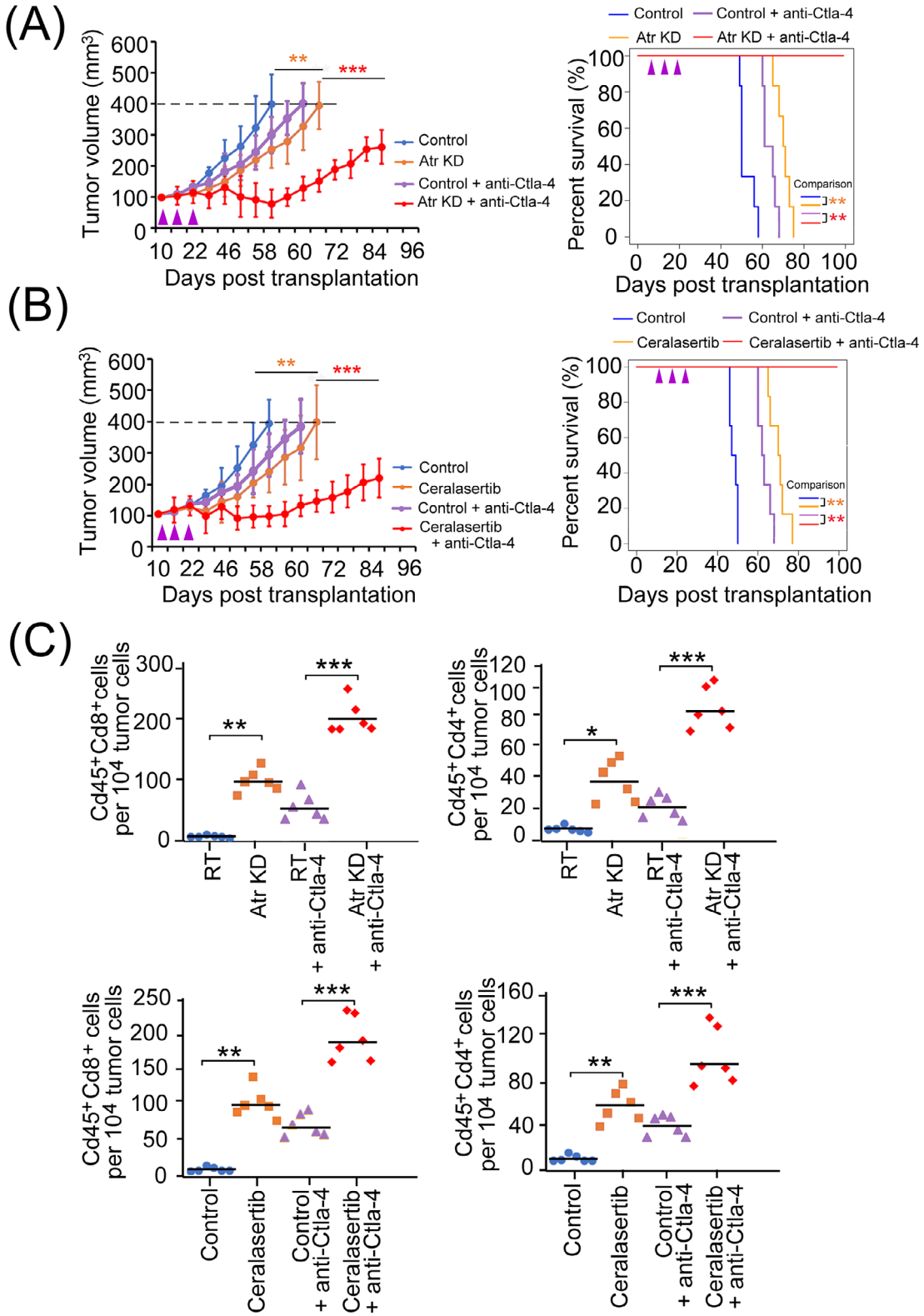

FIGURE 7 **Atr inhibition overcomes the resistance of senescent TRAMP-C1 cells to anti-Ctla-4.** (A) Implanted senescent tumor volume (left panel) and survival analysis (right panel) of control, Atr KD, control + anti-Ctla-4, and Atr KD + anti-Ctla-4 tumors in WT C57BL/6 mice ($n = 6$ for each group). The control group of mice received an equivalent concentration of the mouse IgG2a isotype control antibody. The purple triangle indicates the anti-Ctla-4 injection. (B) Implanted senescent tumor volume (left panel) and survival analysis (right panel) of control, ATRi (ceralasertib, 50 mg/kg), control + anti-Ctla-4, and ATRi + anti-Ctla-4 tumors in WT C57BL/6 mice ($n = 6$ for each group). The control group of mice received an equivalent concentration of the mouse IgG isotype control antibody. The purple triangle indicates the anti-Ctla-4 injection. (C) Quantification of $CD45^+CD8^+$ and $CD45^+CD4^+$ T cells in tumors. Following treatment, the numbers of

an intermediate state rather than the conclusion of RT pressure progression. The two endpoints of the neuroendocrine and proliferative states correspond to the clinical picture of RT-resistant PCa [48, 49]. This fluctuating condition indicated that PCa senescence served as a transitional and varied phase in the advancement toward malignancy (Figure 2). For normal tissue cells, whether cellular senescence is defined as an irreversible and ultimate fate [63] or a transcription factor-driven invertible cell state [64] is debated. In this study, we demonstrated that PCa cellular senescence is a transitional state between the early and advanced stages of cancer cells, which is not indicative of cell death. Given the lack of activation or increase in *PRKDC*, *PARP1*, and *ATM* levels, we concluded that these conditions do not represent a DNA repair process. Additional evidence of this condition included positive β-Gal staining and high expression of *CDKN1A*/*CDKN2A* and SASP-related genes (Figure 2, Supplementary Figure S2B, Supplementary Figure S3B). Once PCa cells enter the senescent state, the fate ends, leading to an advanced cancer status, such as proliferation or a neuroendocrine status, which is consistent with previous reports [65]. Thus, we found that PCa senescence is an intermediate state in which cells escape immune attack for further cancer progression.

In the molecular analysis, ATR was identified as a significantly upregulated gene in the senescent cells. IHC and WB data indicated that the ATR protein levels were elevated in senescent cells. This increase was notably associated with elevated expression of *CDKN1A* and *CDKN2A*, both of which are established indicators of cellular senescence (Figure 3). Moreover, the CD86 protein level was downregulated in senescent cells. Our scRNA-seq and IHC staining data precisely separated the senescent subgroups and indicated that these subgroups presented lower CD86 levels. CD86 loss is a key factor in the insensitivity of cancer cells to anti-CTLA-4 immunotherapy in the clinic [25, 26]. In this study, the findings suggest that RT-induced senescent PCa cells exhibit a lack of CD80 expression and low CD86 expression, indicating a more significant role for CD86 in the immediate senescent state in RT-resistant PCa cells. Similar results were observed in mice, where insensitivity to ICB was due to low levels of CD86, which is consistent with clinical data showing a decrease in $CD8^+$ and $CD4^+$ helper T-cell numbers postradiotherapy [66, 67]. Collectively, these findings indicate that PCa cells undergo senescence as a mechanism to evade immune surveillance, particularly through the downregulation of CD86, which is crucial for immune checkpoint function (Supplementary Figure S8).

As reported, ATR is typically considered an activator in response to DNA damage and DNA replication [50, 51]. The cytosolic function of ATR involves binding to Bid following ultraviolet damage [56]. However, the role of senescence in inducing cytosolic ATR activity in PCa cells remains unexplored. In our study, we revealed a new mechanism for the activation of cytosolic ATR. Western blotting assays demonstrated that senescence influences ATR activity, specifically showing that cytosolic ATR is activated and its expression is elevated in senescent PCa cells induced by RT. Concurrently, nuclear ATR was found to respond to DNA damage caused by RT (Figure 4). A similar phenomenon was observed in senescent hepatic stellate cells, in which senescence upregulated single-stranded DNA accumulation in the cell cytoplasm [68]. The results of a previous study [68] and our data suggested that senescence stimulated cytosolic ATR activation. Moreover, data from the clinical cohort suggested that ATR expression was negatively associated with survival in PCa patients (Supplementary Figure S3D). ATR was also detected in the senescence-specific clusters via scRNA-seq analysis, which revealed a similar early-to-late trajectory of *ATR* expression with respect to senescence marker genes (Figure 2) but not other DNA repair genes, such as *PARP1* and *PRKDC*. More significantly, IHC labeling of the senescent clinical samples revealed low levels of CD86 and high levels of cytosolic ATR (Figure 3). We subsequently excluded the possibility that ATR phosphorylates CD86 via CHK1. Our data indicate that ATR directly targets CD86 in the cytoplasm. A crucial role of protein degradation complexes has been identified in the development of tumors [69], such as immune evasion [70, 71]. Although the domain of CD86 that interacts with the E3 ligase MARCH1 has been previously reported [54, 55], the interaction mechanism and key amino acids involved remain unclear. Using a PTM predictor online, we predicted the ATR phosphorylation sites of CD86. We found that the sites (S279, T286, and T295) of CD86 phosphorylated by ATR were located in the terminal cytoplasmic domain. Interestingly, the cytoplasmic domains of the

infiltrated T cells in the tumors were analyzed by FACS with the corresponding antibodies. The tumors were harvested when they reached a volume of 400 mm^3, except for those in the Atr KD + anti-Ctla-4 and ATRi + anti-Ctla-4 groups. We harvested tumors with a volume of 200 mm^3 from these two groups ($n = 6$ for each group). All the data are presented as the means ± SDs. Tumor volume curves were determined by two-sided Student's t test; survival curves were statistically analyzed with the log-rank test; * $P < 0.05$, ** $P < 0.01$, *** $P < 0.001$, and ns, not significant. Abbreviations: Atr, ataxia telangiectasia and Rad3-related protein; Atri, Atr inhibitor; Ctla-4, cytotoxic T-lymphocyte-associated protein 4; FACS, fluorescence activated cell sorting; KD, knockdown; ns, not significant; SD, standard deviation; WT, wild-type.

MARCH1 protein from both humans and mice contained a conserved RRLK motif (Figure 6). Consequently, phosphorylation by ATR enhanced the electrostatic interaction between MARCH1 and CD86 in the cytoplasm, facilitating the ubiquitination and subsequent degradation of CD86. We further revealed that inhibiting ATR or deleting the RRLK domain increased the efficacy of immunotherapy in mice.

Senescent cells were found in multiple cancers. However, senescent cancer cells induced by RT were hard to be collected in vivo. The reason was that the metastatic cancer was small or disappeared post RT. It was a challenge to collect the samples for senescence staining and scRNA-seq to directly demonstrate the senescent subgroups in vivo. Thus, we used the mice model to mimic the treatment of RT. The limitation of resource post-RT will be solved by new sequencing technology in future.

5 | CONCLUSIONS

Taken together, the results revealed that senescent PCa cells were insensitive to immunotherapy through the specific regulation of CD86. The modification of CD86 by cytosolic ATR enhanced the binding of the E3 ligase MARCH1. The scRNA-seq analysis provided new insights into post-RT progression and the potential mechanism of ICB in PCa. Thus, senescence-related cytosolic ATR might be a potential predictive marker and therapeutic target for combining RT with immunotherapy.

AUTHOR CONTRIBUTIONS

Chenyi Shao, Yyingyi Zhang, Hang Li, Jiajia Chen, Ting Huang, Simeng Wen, Sen Wang and Yu Zhao performed the experiments. Chenyi Shao and Jiaze Li performed the bioinformatic analysis. Jiajia Chen and Simeng Wen collected the patients' samples and provided the patients' tissues and information. Chenyi Shao, Yingyi Zhang, Hang Li, Jiajia Chen and Yu Zhao prepared all the figures and wrote the manuscript. Yu Zhao and Saijun Fan supervised the project. Yu Zhao, Simeng Wen, and Saijun Fan provided funding for the entire project. All the authors read and approved the final manuscript.

ACKNOWLEDGMENTS

We thank the patients and their families for their altruism in participating in the research studies. We thank Dr. Yuanjie Niu (The Second Hospital of Tianjin Medical University, Tianjin China) for providing reagents, plasmids, and PCa tissues. We thank Dr. Ma Jian (Mayo Clinic, Rochester MN) for providing the HA-Ub plasmid. This work was supported in part by grants from the Nonprofit Central Research Institute Fund of the Chinese Academy of Medical Sciences (2021-RC310-010 to Y.Z.), the National Natural Science Foundation of China (81972654 to SM.W. and 81730086 to SJ.F.), the CAMS Innovation Fund for Medical Sciences (2021-I2M-1-042 to SJ.F. and 2021-I2M-1-060 to Y.Z.), and Tianjin International Student Science and Technology Activities (20160014 to SM.W.).

CONFLICT OF INTEREST STATEMENT

The authors declare that they have no conflicts of interest.

DATA AVAILABILITY STATEMENT

All the data that support the findings of this study are available from the corresponding authors upon reasonable request. The single-cell RNA sequencing data were deposited in the GEO database with the accession number GSE234387.

ETHICAL APPROVAL AND CONSENT TO PARTICIPATE

This study was approved by the Laboratory Animal Ethics Committee of the Institute of Radiation Medicine, Chinese Academy of Medical Sciences, under approval number IRM-DWLL-2023033. The study involving patient samples was approved by the Tianjin Medical University Institutional Review Board (ethical approval number: KY2019K036). Written informed consent was obtained from individual participants or their guardians.

ORCID

Yu Zhao https://orcid.org/0000-0002-1242-2257

REFERENCES

1. Shitara K, Ajani JA, Moehler M, Garrido M, Gallardo C, Shen L, et al. Nivolumab plus chemotherapy or ipilimumab in gastro-oesophageal cancer. Nature. 2022;603(7903):942-948.
2. Kraehenbuehl L, Weng CH, Eghbali S, Wolchok JD, Merghoub T. Enhancing immunotherapy in cancer by targeting emerging immunomodulatory pathways. Nat Rev Clin Oncol. 2022;19(1):37-50.
3. Herrera FG, Bourhis J, Coukos G. Radiotherapy combination opportunities leveraging immunity for the next oncology practice. CA Cancer J Clin. 2017;67(1):65-85.
4. Matsumura S, Wang B, Kawashima N, Braunstein S, Badura M, Cameron TO, et al. Radiation-induced CXCL16 release by breast cancer cells attracts effector T cells. J Immunol. 2008;181(5):3099-3107.
5. Ishizuka JJ, Manguso RT, Cheruiyot CK, Bi K, Panda A, Iracheta-Vellve A, et al. Loss of ADAR1 in tumours overcomes resistance to immune checkpoint blockade. Nature. 2019;565(7737):43-48.
6. Postow MA, Callahan MK, Barker CA, Yamada Y, Yuan J, Kitano S, et al. Immunologic correlates of the abscopal effect in a patient with melanoma. N Engl J Med. 2012;366(10):925-931.
7. Formenti SC, Rudqvist NP, Golden E, Cooper B, Wennerberg E, Lhuillier C, et al. Radiotherapy induces responses of lung cancer to CTLA-4 blockade. Nat Med. 2018;24(12):1845-1851.

8. Liu B, Zhang Y, Wang D, Hu X, Zhang Z. Single-cell meta-analyses reveal responses of tumor-reactive CXCL13(+) T cells to immune-checkpoint blockade. Nat Cancer. 2022;3(9):1123-1136.
9. Deng L, Liang H, Xu M, Yang X, Burnette B, Arina A, et al. STING-Dependent Cytosolic DNA Sensing Promotes Radiation-Induced Type I Interferon-Dependent Antitumor Immunity in Immunogenic Tumors. Immunity. 2014;41(5):843-852.
10. Lugade AA, Moran JP, Gerber SA, Rose RC, Frelinger JG, Lord EM. Local radiation therapy of B16 melanoma tumors increases the generation of tumor antigen-specific effector cells that traffic to the tumor. J Immunol. 2005;174(12):7516-7523.
11. Vanpouille-Box C, Alard A, Aryankalayil MJ, Sarfraz Y, Diamond JM, Schneider RJ, et al. DNA exonuclease Trex1 regulates radiotherapy-induced tumour immunogenicity. Nat Commun. 2017;8:15618.
12. Burnette BC, Liang H, Lee Y, Chlewicki L, Khodarev NN, Weichselbaum RR, et al. The efficacy of radiotherapy relies upon induction of type i interferon-dependent innate and adaptive immunity. Cancer Res. 2011;71(7):2488-2496.
13. Herrera FG, Ronet C, Ochoa de Olza M, Barras D, Crespo I, Andreatta M, et al. Low-Dose Radiotherapy Reverses Tumor Immune Desertification and Resistance to Immunotherapy. Cancer Discov. 2022;12(1):108-133.
14. Demaria S, Kawashima N, Yang AM, Devitt ML, Babb JS, Allison JP, et al. Immune-mediated inhibition of metastases after treatment with local radiation and CTLA-4 blockade in a mouse model of breast cancer. Clin Cancer Res. 2005;11(2 Pt 1):728-734.
15. Deng L, Liang H, Burnette B, Beckett M, Darga T, Weichselbaum RR, et al. Irradiation and anti-PD-L1 treatment synergistically promote antitumor immunity in mice. J Clin Invest. 2014;124(2):687-695.
16. Twyman-Saint Victor C, Rech AJ, Maity A, Rengan R, Pauken KE, Stelekati E, et al. Radiation and dual checkpoint blockade activate non-redundant immune mechanisms in cancer. Nature. 2015;520(7547):373-377.
17. Klug F, Prakash H, Huber PE, Seibel T, Bender N, Halama N, et al. Low-dose irradiation programs macrophage differentiation to an iNOS(+)/M1 phenotype that orchestrates effective T cell immunotherapy. Cancer Cell. 2013;24(5):589-602.
18. Dovedi SJ, Adlard AL, Lipowska-Bhalla G, McKenna C, Jones S, Cheadle EJ, et al. Acquired resistance to fractionated radiotherapy can be overcome by concurrent PD-L1 blockade. Cancer Res. 2014;74(19):5458-5468.
19. de Almeida DVP, Fong L, Rettig MB, Autio KA. Immune Checkpoint Blockade for Prostate Cancer: Niche Role or Next Breakthrough? Am Soc Clin Oncol Educ Book. 2020;40:1-18.
20. Lu X, Horner JW, Paul E, Shang X, Troncoso P, Deng P, et al. Effective combinatorial immunotherapy for castration-resistant prostate cancer. Nature. 2017;543(7647):728-732.
21. Alaia C, Boccellino M, Zappavigna S, Amler E, Quagliuolo L, Rossetti S, et al. Ipilimumab for the treatment of metastatic prostate cancer. Expert Opin Biol Ther. 2018;18(2):205-213.
22. Tarhini A, Lin Y, Lin H, Rahman Z, Vallabhaneni P, Mendiratta P, et al. Neoadjuvant ipilimumab (3 mg/kg or 10 mg/kg) and high dose IFN-alpha2b in locally/regionally advanced melanoma: safety, efficacy and impact on T-cell repertoire. J Immunother Cancer. 2018;6(1):112.
23. Kwon ED, Drake CG, Scher HI, Fizazi K, Bossi A, van den Eertwegh AJ, et al. Ipilimumab versus placebo after radiotherapy in patients with metastatic castration-resistant prostate cancer that had progressed after docetaxel chemotherapy (CA184-043): a multicentre, randomised, double-blind, phase 3 trial. Lancet Oncol. 2014;15(7):700-712.
24. Beer TM, Kwon ED, Drake CG, Fizazi K, Logothetis C, Gravis G, et al. Randomized, Double-Blind, Phase III Trial of Ipilimumab Versus Placebo in Asymptomatic or Minimally Symptomatic Patients With Metastatic Chemotherapy-Naive Castration-Resistant Prostate Cancer. J Clin Oncol. 2017;35(1):40-47.
25. Morad G, Helmink BA, Sharma P, Wargo JA. Hallmarks of response, resistance, and toxicity to immune checkpoint blockade. Cell. 2021;184(21):5309-5337.
26. Topalian SL, Taube JM, Anders RA, Pardoll DM. Mechanism-driven biomarkers to guide immune checkpoint blockade in cancer therapy. Nat Rev Cancer. 2016;16(5):275-287.
27. Linsley PS, Ledbetter JA. The role of the CD28 receptor during T cell responses to antigen. Annu Rev Immunol. 1993;11:191-212.
28. Singh S, Lee N, Pedroza DA, Bado IL, Hamor C, Zhang L, et al. Chemotherapy Coupled to Macrophage Inhibition Induces T-cell and B-cell Infiltration and Durable Regression in Triple-Negative Breast Cancer. Cancer Res. 2022;82(12):2281-2297.
29. Constant SL, Bottomly K. Induction of Th1 and Th2 CD4+ T cell responses: the alternative approaches. Annu Rev Immunol. 1997;15:297-322.
30. Colaprico A, Silva TC, Olsen C, Garofano L, Cava C, Garolini D, et al. TCGAbiolinks: an R/Bioconductor package for integrative analysis of TCGA data. Nucleic Acids Res. 2016;44(8):e71.
31. Das A, Fernandez NR, Levine A, Bianchi V, Stengs LK, Chung J, et al. Combined Immunotherapy Improves Outcome for Replication-Repair-Deficient (RRD) High-Grade Glioma Failing Anti-PD-1 Monotherapy: A Report from the International RRD Consortium. Cancer Discov. 2024;14(2):258-273.
32. Love MI, Huber W, Anders S. Moderated estimation of fold change and dispersion for RNA-seq data with DESeq2. Genome Biol. 2014;15(12):550.
33. Xu S, Hu E, Cai Y, Xie Z, Luo X, Zhan L, et al. Using clusterProfiler to characterize multiomics data. Nat Protoc. 2024;19:3292–3320.
34. Weiner AB, Kakani P, Armstrong AJ, Bossi A, Cornford P, Feng F, et al. Risk Stratification of Patients with Recurrence After Primary Treatment for Prostate Cancer: A Systematic Review. Eur Urol. 2024;86(3):200-210.
35. Mukherjee A, Epperly MW, Shields D, Hou W, Fisher R, Hamade D, et al. Ionizing irradiation-induced Fgr in senescent cells mediates fibrosis. Cell Death Discov. 2021;7(1):349.
36. Li L, Yue HC, Han YW, Liu W, Xiong LG, Zhang JW. Relationship between the invasion of lymphocytes and cytokines in the tumor microenvironment and the interval after single brachytherapy hypofractionated radiotherapy and conventional fractionation radiotherapy in non-small cell lung Cancer. BMC Cancer. 2020;20(1):893.
37. Zhang P, Wang D, Zhao Y, Ren S, Gao K, Ye Z, et al. Intrinsic BET inhibitor resistance in SPOP-mutated prostate cancer is mediated by BET protein stabilization and AKT-mTORC1 activation. Nat Med. 2017;23(9):1055-1062.
38. Xu M, Pirtskhalava T, Farr JN, Weigand BM, Palmer AK, Weivoda MM, et al. Senolytics improve physical function and increase lifespan in old age. Nat Med. 2018;24(8):1246-1256.

39. Zhu H, Chen J, Liu K, Gao L, Wu H, Ma L, et al. Human PBMC scRNA-seq-based aging clocks reveal ribosome to inflammation balance as a single-cell aging hallmark and super longevity. Sci Adv. 2023;9(26):eabq7599.
40. Hao Y, Stuart T, Kowalski MH, Choudhary S, Hoffman P, Hartman A, et al. Dictionary learning for integrative, multimodal and scalable single-cell analysis. Nat Biotechnol. 2024;42(2):293-304.
41. Hanzelmann S, Castelo R, Guinney J. GSVA: gene set variation analysis for microarray and RNA-seq data. BMC Bioinformatics. 2013;14:7.
42. Aran D. Cell-Type Enrichment Analysis of Bulk Transcriptomes Using xCell. Methods Mol Biol. 2020;2120:263-276.
43. Ntala C, Salji M, Salmond J, Officer L, Teodosio AV, Blomme A, et al. Analysis of Prostate Cancer Tumor Microenvironment Identifies Reduced Stromal CD4 Effector T-cell Infiltration in Tumors with Pelvic Nodal Metastasis. European Urology Open Science. 2021;29:19-29.
44. Wen S, Wei Y, Zen C, Xiong W, Niu Y, Zhao Y. Long non-coding RNA NEAT1 promotes bone metastasis of prostate cancer through N6-methyladenosine. Mol Cancer. 2020;19(1):171.
45. Zhao Y, Ding L, Wang D, Ye Z, He Y, Ma L, et al. EZH2 cooperates with gain-of-function p53 mutants to promote cancer growth and metastasis. EMBO J. 2019;38(5):e99599.
46. Zhao Y, Li H, Zhang Y, Li L, Fang R, Li Y, et al. Oncoprotein HBXIP Modulates Abnormal Lipid Metabolism and Growth of Breast Cancer Cells by Activating the LXRs/SREBP-1c/FAS Signaling Cascade. Cancer Res. 2016;76(16):4696-4707.
47. Zhang DKY, Cheung AS, Mooney DJ. Activation and expansion of human T cells using artificial antigen-presenting cell scaffolds. Nat Protoc. 2020;15(3):773-798.
48. Chen S, Zhu G, Yang Y, Wang F, Xiao YT, Zhang N, et al. Single-cell analysis reveals transcriptomic remodellings in distinct cell types that contribute to human prostate cancer progression. Nat Cell Biol. 2021;23(1):87-98.
49. Park JW, Lee JK, Sheu KM, Wang L, Balanis NG, Nguyen K, et al. Reprogramming normal human epithelial tissues to a common, lethal neuroendocrine cancer lineage. Science. 2018;362(6410):91-95.
50. Saxena S, Zou L. Hallmarks of DNA replication stress. Mol Cell. 2022;82(12):2298-2314.
51. Toledo LI, Altmeyer M, Rask MB, Lukas C, Larsen DH, Povlsen LK, et al. ATR prohibits replication catastrophe by preventing global exhaustion of RPA. Cell. 2013;155(5):1088-1103.
52. Huang W, Hickson LJ, Eirin A, Kirkland JL, Lerman LO. Cellular senescence: the good, the bad and the unknown. Nat Rev Nephrol. 2022;18(10):611-627.
53. Cleary JM, Aguirre AJ, Shapiro GI, D'Andrea AD. Biomarker-Guided Development of DNA Repair Inhibitors. Mol Cell. 2020;78(6):1070-1085.
54. Corcoran K, Jabbour M, Bhagwandin C, Deymier MJ, Theisen DL, Lybarger L. Ubiquitin-mediated regulation of CD86 protein expression by the ubiquitin ligase membrane-associated RING-CH-1 (MARCH1). J Biol Chem. 2011;286(43):37168-37180.
55. Liu H, Wilson KR, Firth AM, Macri C, Schriek P, Blum AB, et al. Ubiquitin-like protein 3 (UBL3) is required for MARCH ubiquitination of major histocompatibility complex class II and CD86. Nat Commun. 2022;13(1):1934.
56. Hilton BA, Li Z, Musich PR, Wang H, Cartwright BM, Serrano M, et al. ATR Plays a Direct Antiapoptotic Role at Mitochondria, which Is Regulated by Prolyl Isomerase Pin1. Mol Cell. 2015;60(1):35-46.
57. Shi Y, Li H, Chu D, Lin W, Wang X, Wu Y, et al. Rescuing Nucleus Pulposus Cells From Senescence via Dual-Functional Greigite Nanozyme to Alleviate Intervertebral Disc Degeneration. Adv Sci (Weinh). 2023;10(25):e2300988.
58. Li Q, Zhao YH, Xu C, Liang YL, Zhao Y, He QM, et al. Chemotherapy-Induced Senescence Reprogramming Promotes Nasopharyngeal Carcinoma Metastasis by circRNA-Mediated PKR Activation. Adv Sci (Weinh). 2023;10(8):e2205668.
59. Trenker R, Wu X, Nguyen JV, Wilcox S, Rubin AF, Call ME, et al. Human and viral membrane-associated E3 ubiquitin ligases MARCH1 and MIR2 recognize different features of CD86 to downregulate surface expression. J Biol Chem. 2021;297(1):100900.
60. Shi X, Yang Y, Zhang W, Wang J, Xiao D, Ren H, et al. FLASH X-ray spares intestinal crypts from pyroptosis initiated by cGAS-STING activation upon radioimmunotherapy. Proc Natl Acad Sci U S A. 2022;119(43):e2208506119.
61. Paffenholz SV, Salvagno C, Ho YJ, Limjoco M, Baslan T, Tian S, et al. Senescence induction dictates response to chemo- and immunotherapy in preclinical models of ovarian cancer. Proc Natl Acad Sci U S A. 2022;119(5):e2117754119.
62. Berger G, Knelson EH, Jimenez-Macias JL, Nowicki MO, Han S, Panagioti E, et al. STING activation promotes robust immune response and NK cell-mediated tumor regression in glioblastoma models. Proc Natl Acad Sci U S A. 2022;119(28):e2111003119.
63. Baker DJ, Childs BG, Durik M, Wijers ME, Sieben CJ, Zhong J, et al. Naturally occurring p16(Ink4a)-positive cells shorten healthy lifespan. Nature. 2016;530(7589):184-189.
64. Yang JH, Hayano M, Griffin PT, Amorim JA, Bonkowski MS, Apostolides JK, et al. Loss of epigenetic information as a cause of mammalian aging. Cell. 2023;186(2):305-326 e27.
65. Owens JL, Beketova E, Liu S, Shen Q, Pawar JS, Asberry AM, et al. Targeting Protein Arginine Methyltransferase 5 Suppresses Radiation-induced Neuroendocrine Differentiation and Sensitizes Prostate Cancer Cells to Radiation. Mol Cancer Ther. 2022;21(3):448-459.
66. Rudqvist NP, Pilones KA, Lhuillier C, Wennerberg E, Sidhom JW, Emerson RO, et al. Radiotherapy and CTLA-4 Blockade Shape the TCR Repertoire of Tumor-Infiltrating T Cells. Cancer Immunol Res. 2018;6(2):139-150.
67. Oweida AJ, Darragh L, Phan A, Binder D, Bhatia S, Mueller A, et al. STAT3 Modulation of Regulatory T Cells in Response to Radiation Therapy in Head and Neck Cancer. J Natl Cancer Inst. 2019;111(12):1339-1349.
68. Takahashi A, Loo TM, Okada R, Kamachi F, Watanabe Y, Wakita M, et al. Downregulation of cytoplasmic DNases is implicated in cytoplasmic DNA accumulation and SASP in senescent cells. Nat Commun. 2018;9(1):1249.
69. Bouchard JJ, Otero JH, Scott DC, Szulc E, Martin EW, Sabri N, et al. Cancer Mutations of the Tumor Suppressor SPOP Disrupt the Formation of Active, Phase-Separated Compartments. Mol Cell. 2018;72(1):19-36. e8.
70. Wang X, Tokheim C, Gu SS, Wang B, Tang Q, Li Y, et al. In vivo CRISPR screens identify the E3 ligase Cop1 as a modulator of

macrophage infiltration and cancer immunotherapy target. Cell. 2021;184(21):5357-5374. e22.

71. Gu SS, Zhang W, Wang X, Jiang P, Traugh N, Li Z, et al. Therapeutically Increasing MHC-I Expression Potentiates Immune Checkpoint Blockade. Cancer Discov. 2021;11(6):1524-1541.

SUPPORTING INFORMATION

Additional supporting information can be found online in the Supporting Information section at the end of this article.

How to cite this article: Shao C, Zhang Y, Li H, Chen J, Huang T, Li J, et al. Radiotherapy-resistant prostate cancer cells escape immune checkpoint blockade through the senescence-related ataxia telangiectasia and Rad3-related protein. Cancer Commun. 2024;1–27.
https://doi.org/10.1002/cac2.12636